Crude Closure for Flow with Topography Through Large Scale Statistical Theory

M.J. Grote and A.J. Majda[1]

[1]Courant Institute of Mathematical Sciences, New York University, 251 Mercer Street, New York, NY 10012, USA

Crude Closure for Flow with Topography Through Large Scale Statistical Theory

M.J. Grote and A.J. Majda[1]

Seminar für Angewandte Mathematik
Eidgenössische Technische Hochschule
CH-8092 Zürich
Switzerland

Abstract

Crude closure algorithms based on equilibrium statistical theories are developed here for prototypical geophysical flows involving barotropic flow over topography. These crude closure algorithms are developed utilizing the simplest energy-enstrophy statistical theory for flow with topography; in these algorithms, only a single parameter, the energy, is tracked by the algorithm and the entire flow structure is predicted through the equilibrium statistical state. In particular, no explicit parametrization of a sub-grid scale energy spectrum is utilized in the algorithm. The predictions of the crude closure algorithm are compared with direct pseudo-spectral numerical simulations of the barotropic flow equations with random small scale forcing and dissipation for a variety of random topographies in basin, channel, and periodic geometries. In most situations studied here, the energy is tracked within small errors by the crude closure while the velocity errors rarely exceed 10% provided that the enstrophy/energy ratio is not large or growing significantly in time. Examples are also introduced where the crude closure algorithm based on the energy enstrophy theory fails; in these circumstances, a crude closure algorithm based on more sophisticated equilibrium statistical theories is introduced as a possible remedy.

---

[1]Courant Institute of Mathematical Sciences, New York University, 251 Mercer Street, New York, NY 10012, USA

1 Introduction

The tendency of turbulent geophysical flows to display two-dimensional behavior and self-organize into coherent structures has been reported numerous times from physical observations and numerical simulations ([1, 2]). Various equilibrium statistical theories have been proposed to provide a mathematical framework underpinning the well-known emergence of coherent structures in freely evolving two-dimensional flow. These theories apply to inviscid and unforced flow and attempt to predict the large time behavior as it approaches statistical equilibrium. Both the infinite number of degrees of freedom and the infinite number of conserved integrals preclude the direct use of classical statistical mechanics to two-dimensional flow. As a result various statistical theories have been proposed, which differ from each other mainly by their individual choice of conserved quantities and the "discretization" procedure used to represent the continuum by a countable set of "particles" (spectral representation, point-vortices, lattice models, etc.) Examples are the energy-enstrophy theory ([3, 4]), the point-vortex theory ([5, 6, 7, 8]), the Miller-Robert theory ([9, 10, 11]), and a very recent few constraint statistical theory based on extrema of the potential vorticity ([12, 13]). Each statistical theory yields a different relationship between the vorticity and the stream function, which defines a coarse-grained (macroscopic) description of the steady flow at statistical equilibrium, superimposed with local random fluctuations.

Rigorous theory [14] establishes that the large scale statistical macrostates of the Miller-Robert theory, involving infinitely many constraints, preserve only the energy, the circulation, and perhaps the extrema of the typical microstate vorticity. This fact suggests that, in some contexts, utilizing only a few judicious constraints might be simpler and more appropriate. Furthermore, real flows are neither inviscid nor freely evolving, so that such higher order equilibrium statistics based on inviscid dynamics is rapidly lost in time. Additional evidence is provided by a numerical study in ref. [14], which shows that for viscous decaying flow, even the simplest statistical theories accurately describe the overall evolution of the time dependent flow. These encouraging results lead the authors [15] to devise crude closure algorithms based on few constraint statistical theories. These algorithms involve the nonlinear evolution of a few parameters, such as the energy and the circulation. They are designed through enforcing the following two assumptions:

1) All dissipation of energy and circulation occurs in the large scale statistical flow.

2) The effect of small scale forcing is to instantaneously change the large scale statistical structure to a new large scale statistical structure with an adjusted energy and circulation.

The crude closure algorithms displayed remarkably accurate and robust predictive ability of the large scale behavior of damped flow driven by small scale random forcing in a basin, even under harsh conditions where all assumptions underlying equilibrium statistical theories are clearly violated [15] and without any turbulence parametrization for the inverse cascade process.

The development of crude closure models for fluid flows which exhibit organized large scale structure, such as geophysical flows, remains an important practical issue. Especially the evolution of large scale ocean flow remains a formidable challenge and necessitates the modeling of unresolved eddy motion. Simulations by Holloway ([16, 17]) indicate that subscale modeling based on statistical mechanics leads to substantial improvement in model fidelity without incurring the cost of eddy resolution. Holloway suggests that the unresolved eddies are not a damping of the ocean circulation but rather a systematic driving force which tends to move the model to higher entropy states. In contrast, conventional eddy-viscosity models tend to drag the numerical solution toward a state of rest.

Barotropic flows over topography are the simplest prototype geophysical flows where even the simplest energy-enstropy statistical theory yields striking predictions for a "most probable state" mean flow ([4, 18]). The emergence of such states as averages over large time intervals in damped and driven numerical simulations has been studied extensively with many interesting results ([1, 19, 20, 21, 22]). Here, in a complementary direction, we devise and test crude closure algorithms based on the energy-enstrophy statistical theory where the entire closure is based on a single predicted evolving parameter, the energy.

In Section 2, we extend crude closure algorithms presented by the authors in [15] to barotropic flow over topography. The simplest algorithm involves the nonlinear evolution of a single parameter, the energy, for dynamic closure based on the energy-enstrophy statistical theory. The crude closure algorithm is tested for damped flow over random topography, driven by random small scale forcing in three different domains: the basin, the channel, and periodic geometry. Crude closure based on the inclusion of a second parameter, the circulation, is also discussed briefly. In Section 3, we test the crude dynamic closure theory developed in Section 2 on solutions of the barotropic flow equations over random topography defined on a rectangular domain with stress-free boundary conditions and with strong small scale forcing at moderately large Reynolds numbers. We test the crude dynamic closure algorithms under increasingly stringent conditions ranging from freely decaying flows to spin-up from rest by random forcing with like signed vortices, and finally to random forcing by vortices with alternating or opposite sign. We compare standard 128^2 spectral code numerical simulations with crude dynamic closure based upon only a single evolving parameter in the energy-enstrophy theory. In all cases the energy is tracked with such accuracy, that the predicted value can hardly be distinguished from the exact energy. In Section 4 we perform a study analogous to that in Section 3 but for flow in a channel. The numerical results corroborate the previous results and demonstrate the ability of the crude dynamic closure to cross violent changes in flow topology, as the flow reorganizes from a flow regime dominated by topography to a regime dominated by relative vorticity. Section 5 involves a similar study for flow in double periodic geometry. Finally in Section 6, we point out the limitations of the crude closure based on the simple energy-enstrophy theory via a special low-energy dynamic transition over two-mode layered topography, which the crude closure fails to predict. Additional results suggest the potential benefit from using a recent more sophisticated statistical theory ([12, 13]), which involve only a few additional conserved quantities.

2 Crude closure dynamics

We consider the barotropic flow equations with damping and driving over topography in a two-dimensional region Ω,

$$\frac{\partial q}{\partial t} + \vec{v} \cdot \nabla q = P_0(\Delta)\omega + F. \tag{1}$$

Here $\vec{v}(x, y, t)$ denotes the velocity, $q(x, y, t)$ the potential vorticity, and $\omega(x, y, t)$ the relative vorticity of the flow. They are related to each other via the stream function ψ by

$$\vec{v} = \nabla^{\perp}\psi = \left(-\frac{\partial \psi}{\partial y}, \frac{\partial \psi}{\partial x}\right), \tag{2}$$

$$\omega = \Delta\psi, \tag{3}$$

$$q = \omega + h, \tag{4}$$

where $h(x, y)$ defines the underlying topography. Dissipative effects are incorporated through the viscous operator $P_0(\Delta)$ defined by

$$P_0(\Delta)\,\omega = -d\,\omega + \nu\Delta\,\omega + \nu_H\Delta^3\omega. \tag{5}$$

The viscous operator includes the Ekman drag coefficient, d, the Newtonian viscosity coefficient, ν, and the hyperviscosity coefficient, ν_H. Higher order effects could easily be incorporated. The first two dissipation mechanisms are radically different from each other. While Ekman drag models the effects of boundary layers in large scale geophysical flows and dissipates energy at all scales equally, Newtonian viscosity corresponds to molecular or turbulent diffusion and dissipates much more strongly the smaller scales. Frequently used in geophysical applications, the main role of hyperviscosity in the present discussion is to guarantee numerical stability in situations where we set $\nu = 0$ in (5) (see sections 3.3, 4.2, and 5). We choose the forcing F to mimic a random bombardment of the flow with localized smoothed vortices of radius r,

$$F = \sum_{j \geq 1} \delta(t - t_j)\omega_r(\vec{x} - \vec{x}_j). \tag{6}$$

The bounded domain Ω stands for the periodic box, the basin, or the channel. If $\Omega = [0, 2\pi) \times [0, 2\pi)$ is the periodic box (torus), both ψ and h are 2π-periodic in x and y, and we assume that their integrals over Ω vanish. Alternatively, if $\Omega = [0, 2\pi) \times [0, \pi]$ is the channel, ψ and h are 2π-periodic in x and satisfy free-slip boundary conditions at the upper and lower boundaries $y = 0, \pi$,

$$\frac{\partial^{2p}}{\partial y^{2p}}\psi(x, y, t) = 0, \qquad y = 0, \pi, \qquad p = 0, 1, 2, 3. \tag{7}$$

Finally, if $\Omega = [0, \pi] \times [0, \pi]$ is the basin, neither ψ nor h are periodic; hence, we impose free-slip boundary conditions over the entire boundary of Ω,

$$\frac{\partial^{2p}}{\partial n^{2p}}\psi(x, y, t) = 0, \qquad p = 0, 1, 2, 3, \tag{8}$$

3

where n is normal to the boundary of Ω. In the absence of topography and Ekman drag, $h(x, y) = 0$ and $d = 0$, the barotropic flow equations (1) reduce to the two-dimensional Navier-Stokes equations.

At any time t the energy E, the enstrophy $\mathcal{E}$, and the circulation Γ are given by

$$E(t) \;=\; \frac{1}{2}\fint |\vec{v}|^2 = -\frac{1}{2}\fint \omega\psi, \tag{9}$$

$$\mathcal{E}(t) \;=\; \frac{1}{2}\fint q^2, \tag{10}$$

$$\Gamma(t) \;=\; \fint q. \tag{11}$$

Here the horizontal bar across the integral sign indicates normalization with respect to the area of Ω. In the absence of forcing and vicous effects ($F = 0$ and $P_0(\Delta) \equiv 0$), the barotropic flow equations (1) conserve the energy, the enstrophy, the circulation, as well as the infinite number of integrals involving any arbitrary nonlinear function G of the potential vorticity,

$$\fint G(q). \tag{12}$$

Given a subset of conserved quantities what is the most probable flow configuration, q^*, at statistical equilibrium ? Various statistical theories have been proposed to answer this question. These theories differ from each other through their individual choice of conserved quantities. Typically, they yield a nonlinear elliptic *mean-field equation*, which relates the coarse-grained potential vorticity field, q^*, to its corresponding stream function ψ^* via

$$q^* = f(\psi^*; E, \Gamma, \ldots), \qquad q^* = \Delta\psi^* + h. \tag{13}$$

The stream lines of these mean flows are smooth across Ω; they ignore small scale fluctuations and thus correspond to large-scale coherent structures in the flow. Because of topography they can contain small scale features, in particular at low energy. Since equation (13) implies that

$$\nabla^{\perp}\psi^* \cdot \nabla q^* = 0, \tag{14}$$

any such mean flow is an exact steady-state solution of the inviscid and unforced barotropic flow equations (1).

2.1 Energy-Enstrophy theories

The simplest non-trivial relation between q^* and ψ^* is linear and results from the energy-enstrophy theory for two-dimensional inviscid flow over topography. This equilibrium statistical theory starts from a truncated spectral representation of the equations of motion (1) in the absence of forcing and viscosity. Instead of the infinite number of conserved integrals in (12), the truncated dynamics then conserve only the energy and the enstrophy. By maximizing the entropy of this finite dimensional dynamical system, Salmon, Holloway, and Hendershott [4] derive the mean-field equation

$$q^* = \mu\psi^*, \tag{15}$$

4

where μ is a Lagrange multiplier determined by the energy. Since the integral of h vanishes, equation (15) has a unique solution for all $\mu > -\lambda_1$, where $\lambda_1 > 0$ is the lowest eigenvalue of the Laplacian in Ω – recall that zero is not an eigenvalue because we have assumed that the integral of ψ vanishes. For a given energy there are in general multiple stationary solutions of (15) for different values of μ. Yet only the steady-states that lie on the branch $\mu > -\lambda_1$ are nonlinearly stable and thus are the most physically relevant; moreover, they minimize the potential enstrophy for given energy ([19]). Carnevale and Frederiksen [18] show that in the limit of infinite resolution the canonical equilibrium is statistically sharp and identical to the nonlinearly stable minimum enstrophy state. In summary, for every value of the energy $E > 0$ there is a unique value $\mu > -\lambda_1$, which determines the nonlinearly stable steady state via (15).

Let us assume that the flow is initially at statistical equilibrium, which is completely defined by its energy. As time progresses, the flow evolves under the constant action of small scale forcing and dissipation. With the addition of every new localized vortex, the energy slightly changes, thereby forcing the large scale flow into a new statistical state with adjusted energy. In the absence of forcing, the energy decreases because of dissipative effects; we estimate the decay in energy by assuming that all dissipation occurs in the large scales of the flow. This strategy leads to the crude closure algorithm, which captures the large-scale behavior of the damped and driven flow only by tracking the energy without actually solving the fluid equations.

As the flow evolves under the constant bombardment with localized vortices, it alternates between two extreme flow regimes: a phase of applied forcing and a phase of pure decay.

Applied forcing
We begin with the addition of a single vortex ω at $t = \bar{t}$ to the current approximate state $\bar{\omega}$ of the flow. Let $\bar{t}_-$ denote the instant just before and $\bar{t}_+$ the instant right after the event. Then

$$\psi_{\bar{t}_+} = \bar{\psi}_{\bar{t}_-} + \psi, \tag{16}$$

$$\omega_{\bar{t}_+} = \bar{\omega}_{\bar{t}_-} + \omega. \tag{17}$$

How much does E increase in time from adding a vortex at $\bar{t}$? By using equations (16) and (17) in equation (5), we immediately obtain

$$E(\bar{t}_+) = E(\bar{t}_-) - \oint \bar{\psi}\omega - \frac{1}{2}\oint \psi\omega. \tag{18}$$

Since $\bar{\psi}$, ω, and ψ are explicitly known, we can evaluate the right-hand sides of (18) and thus update the energy. This new value of E defines the new state $\bar{\omega}$ of the approximate solution via (15), with μ uniquely determined by E.

Pure decay
Let Δt denote the time interval between forcing by two successive random vortices. Given the approximate solution $\bar{\omega}$ at $t = \bar{t}_+$, we need to determine the evolution of the approximate dynamics during the decay phase, $\bar{t}_+ \leq t < \bar{t} + \Delta t$, up to the instant just before adding the next localized vortex, $t = \bar{t} + \Delta t$. To do so, we must determine the change in energy and circulation in a situation without forcing.

Since we do not have simple exact expressions that describe the evolution of E and Γ we need to estimate their change during decay. At the equilibrium statistical state defined by the closure algorithm at $\bar{t}_+$, the nonlinear terms in (1) vanish identically, Thus, we approximate the evolution of q over $\bar{t}_+ \leq t < \bar{t} + \Delta t$ by

$$\frac{\partial q}{\partial t} = P_0(\Delta)\omega. \tag{19}$$

The solution reduces to the first-order Taylor approximation

$$\begin{aligned}
\tilde{\omega} &= \bar{\omega} + (t - \bar{t})P_0(\Delta)\bar{\omega}, \\
\tilde{\psi} &= \bar{\psi} + (t - \bar{t})P_0(\Delta)\bar{\psi}.
\end{aligned} \tag{20}$$

To estimate the change in the energy, we remark that

$$\dot{E} = -\int \psi \frac{\partial \omega}{\partial t}.$$

Since at $t = \bar{t}$ we have $\partial_t \omega = P_0(\Delta)\omega$, we approximate the change in energy over $(\bar{t}, \bar{t} + \Delta t)$ by

$$\begin{aligned}
\dot{E} &= -\int \tilde{\psi} P_0(\Delta)\tilde{\omega} \tag{21} \\
&= -\int [\bar{\psi} + (t - \bar{t})P_0(\Delta)\bar{\psi}][P_0(\Delta)(\bar{\omega} + (t - \bar{t})P_0(\Delta)\bar{\omega})]. \tag{22}
\end{aligned}$$

Integrating in time up to $t = t + \Delta t$ yields the following estimate for the change in the energy,

$$\begin{aligned}
E(t + \Delta t) &= E(t) - \Delta t \int \bar{\psi} P_0(\Delta)\bar{\omega} - \frac{(\Delta t)^2}{2} \int [P_0(\Delta)\bar{\psi}][P_0(\Delta)\bar{\omega}] \tag{23} \\
&\quad - \frac{(\Delta t)^2}{2} \int \bar{\psi}[P_0(\Delta)^2\bar{\omega}] - \frac{(\Delta t)^3}{3} \int [P_0(\Delta)\bar{\psi}][P_0(\Delta)^2\bar{\omega}]. \tag{24}
\end{aligned}$$

For the sake of clarity, we summarize the crude closure algorithm below.

Crude closure algorithm:

0. At $t = 0$ match $\bar{E}$ with the energy of the initial flow. This defines the initial approximate statistical state $\bar{q} = \bar{\omega} + h = \mu\bar{\psi}$.

1. Let $\bar{E}_-$ denote the current approximate energy, which defines the statistical state $\bar{q} = \mu\bar{\psi}$ at $t = \bar{t}_-$. Compute the change in $\bar{E}$ due to the addition of a localized vortex ω,

$$\bar{E}_+ = \bar{E}_- - \int \bar{\psi}\omega - \frac{1}{2}\int \psi\omega. \tag{25}$$

This defines the new statistical state $\bar{\omega}$ at $t = \bar{t}_+$ via $\bar{q} = \mu\bar{\psi}$ with the energy $\bar{E}_+$.

2. Compute the change in $\bar{E}$ during decay, $\bar{t} < t < t + \Delta t$:

$$
\begin{aligned}
E(t + \Delta t) \quad = \quad & E(t) - \Delta t \int \bar{\psi} P_0(\Delta) \bar{\omega} - \frac{(\Delta t)^2}{2} \int [P_0(\Delta)\bar{\psi}][P_0(\Delta)\bar{\omega}] \\
& - \frac{(\Delta t)^2}{2} \int \bar{\psi}[P_0(\Delta)^2 \bar{\omega}] - \frac{(\Delta t)^3}{3} \int [P_0(\Delta)\bar{\psi}][P_0(\Delta)^2 \bar{\omega}]. \quad (26)
\end{aligned}
$$

This defines the new statistical state $\bar{q}$ at $t = \bar{t} + \Delta t$.

3. Return to 1.

We emphasize that the crude closure algorithm marches in time independently and without any knowledge of the solution of (1). It only requires the initial energy at $t = 0$, the applied external forcing, and the values of the various dissipation coefficients.

2.2 More complex few constraint statistical theories

The crude closure algorithm presented in the previous section utilizes mean states, which are completely determined by the energy. A natural extension consists in including additional quantities from the infinite number of integrals conserved by the inviscid and unforced dynamics (12). This leads to a richer family of mean states and thus can possibly result in a crude closure, which adapts to a wider range of flow situations.

For example, the statistical theory with both the energy and the circulation has a mean field equation which reduces to the *linear* elliptic equation,

$$
\Delta \psi^* + h = q^* = \mu \psi^* + \alpha. \tag{27}
$$

Here μ and α are Lagrange multipliers uniquely determined by the energy E_0 and the circulation Γ_0. Again for each pair (μ, α) there is a unique solution to (27) for $\mu > -\lambda_1$, the smallest nonzero eigenvalue of the Laplacian in Ω. Thus we have obtained a richer two-parameter family of statistical states. When the circulation constraint is absent, α vanishes and we recover the mean-field equation of the energy-enstrophy theory (15). Since the circulation of any flow in periodic geometry is identically zero, $\alpha = 0$ and the one- and two-parameter crude closure algorithms coincide in this special situation. Although we have implemented and tested the crude closure based on the above two-parameter family of statistical states, we omit showing these numerical results here for two reasons. First, in the majority of numerical experiments the results from the one-parameter crude closure are so accurate that the additional improvement provided by $\bar{\Gamma}$ is negligible. Second, to accommodate the special flow configurations over layered topography presented in Section 6, the mean-field equation must be nonlinear, unlike (27).

The addition of the circulation constraint besides the energy to the maximization of the entropy does not lead to any significant improvement in the performance of the crude closure. However, the addition of a few judiciously chosen constraints from the infinite list in [12] might improve the performance of the crude closure

algorithm significantly. We present such an example in Section 6 below. Following Turkington [12] and DiBattista, Majda, and Turkington [13], we utilize the extrema of the potential vorticity as the additional conserved quantities besides the energy. Let Q_+ and Q_- denote the maximum and the minimum respectively of the initial potential vorticity field, where $Q = (Q_+ - Q_-)/2$ and $\bar{Q} = (Q_+ + Q_-)/2$ are the half-width and midpoint of the interval $[Q_-, Q_+]$ respectively. By repeating the calculations in [12] and [13], the mean-field equation in this setting becomes

$$\Delta\psi + h = q = \bar{Q} + Q\mathcal{L}[Q(\theta\psi - \gamma)], \quad \text{where} \quad \mathcal{L}[z] = \coth z - \frac{1}{z} \qquad (28)$$

is the classical Langevin function. Again θ and γ are Lagrange multipliers associated with the energy and the circulation constraints. In contrast to the mean-field equation in (27), the mean-field equation in (28) is *nonlinear*; it involves two additional parameters, Q_+ and Q_-. Therefore it yields a richer family of statistical states. To compute the entropy maximizing probability distribution, ρ^*, for given E_0, Γ_0, Q_+, and Q_-, we use the algorithm developed by Turkington and Whitaker [20]. This approach is based on the Kuhn-Tucker formulation of the above constrained optimization problem and proceeds by successive linearization of the energy constraint. DiBattista, Majda, and Turkington [13] extended this procedure to a nonzero mean flow with beta-effect and explored flow configurations spanned by the entire parameter space. In particular they identified the parameter regimes for which the entropy maximizing flow in a channel without topography bifurcates from a ubiquitous shear flow to a monopolar vortex. In Section 6 we trivially modify this algorithm for flow over topography and determine the mean-field potential vorticity, q^*, defined by the entropy maximizer ρ^*.

2.3   Diagnostics

We shall compare the "exact" (numerical) solution with two types of approximate statistical states. On the one hand, we shall verify the *consistency* of the equilibrium statistical theories in a non-equilibrium regime simply by matching the instantaneous exact energy E of the flow. Thus, given the exact computed value of E, we compare the statistical state $q^* = \mu^*\psi^*$ with the exact solution q, where μ^* is determined by $\mathcal{E}$. On the other hand, we shall measure the *accuracy* of the crude dynamic closure by comparing the approximate statistical state $\bar{q}$, defined above by the crude dynamics algorithm, with the exact solution q. Although one might initially be lead to believe that the macrostates obtained by matching E to those of the exact solution would give much better results, we will provide ample numerical evidence that this is not so. On the contrary, because the evolution of bulk features in the flow, such as the energy, will prove to be remarkably well-predicted, even under harshest conditions, by the crude closure algorithm, both error measures based either on accuracy or on consistency tend to agree extremely well; in fact, it is usually quite difficult to distinguish between them in any given situation.

To verify the consistency of the equilibrium statistical theory, we need to compare in a quantitative fashion how close the instantaneous vorticity q and its corresponding stream function ψ come to satisfying (13). We introduce the correlation function

of f and g

$$\text{Corr}(f, g) = 1 - \frac{(f, g)^2}{\|f\|^2 \|g\|^2}, \tag{29}$$

where (f, g) denotes the L_2-inner product on Ω and $\|f\|_2$ its corresponding L_2-norm. We recall that the correlation satisfies $0 \leq \text{Corr}(f, g) \leq 1$ and that the correlation is zero if and only if f and g are collinear, that is

$$\text{Corr}(f, g) = 0 \qquad \Longleftrightarrow \quad f(x, y) = c\, g(x, y), \ \text{ for some constant } c \neq 0. \tag{30}$$

Thus we calculate $\text{Corr}(q, \psi)$ to measure how well q satisfies (10).

To calculate the accuracy of the crude closure algorithm, we must compare the exact solution q either with the macrostate q^*, where E is simply matched to the exact solution, or with the statistical state $\bar{q}$, which is defined by (9) with $\bar{E}$ determined by the crude closure algorithm described above. We shall use two different error measures, the relative L_2-error in the vorticity,

$$\text{Err}(q, q^*) = \frac{\|q(t, .) - q^*(t, .)\|_2}{\|q(t, .)\|_2}, \tag{31}$$

and the relative L_2-error in the velocity,

$$\text{Err}(\vec{v}, \vec{v^*}) = \frac{\|\vec{v}(t, .) - \vec{v^*}(t, .)\|_2}{\|\vec{v}(t, .)\|_2}. \tag{32}$$

Both error measures quantify the relative closeness of either statistical state, $\bar{q}$ or q^*, to the exact solution, q. Since we are strongly perturbing the flow with random localized vortices, we expect larger errors in the vorticity. Indeed (31) is a very tough measure of the relative closeness between two solutions of (1)–(4) with random forcing; in particular when $\nu = 0$ there is no inherent dissipative mechanism but hyperviscosity to remove small scales in the flow.

The following two diagnostic quantities, both enstrophy-energy ratios, will prove useful in assessing the range of validity of the crude closure:

$$\Lambda(t) = \frac{\int \omega^2}{\int |\nabla \psi|^2}, \tag{33}$$

$$\Lambda_q(t) = \frac{\int q^2}{\int |\nabla \psi|^2}. \tag{34}$$

Note that both Λ and Λ_q have the units, $(\text{length})^{-2}$. We use Λ as a measure of the roughness of the flow, whereas $\sqrt{\Lambda_q}$ provides an average inverse length scale. In any given situation, the magnitude of Λ_q will prove a clear indicator for the performance of the crude closure, with improved performance at lower values. Although strongly perturbed flows often produce large relative errors in velocity, the crude closure algorithm is usually able to track the evolution of bulk features of the flow quite accurately, as long as Λ_q is not too big. Large values of Λ_q indicate little if no inverse energy cascade and as a result no emergence of large coherent structures.

The large scale Reynolds number, Re, is defined as

$$Re = \frac{L\, |\vec{v}|_{\max}}{\nu}, \tag{35}$$

where $L = 2\pi$ for the torus or the channel, and $L = \pi$ for the basin.

2.4 Numerical method

We solve the barotropic flow equations (1) numerically on a 2π-periodic domain with a pseudo-spectral method. Thus we compute the spatial derivatives $\vec{v} = \nabla^{\perp}\psi$ and $\nabla\vec{q}$ in Fourier space, but then evaluate the product $\vec{v}\cdot\nabla\vec{q}$ in physical space. The numerical scheme proceeds in time by using a split-step procedure, where the diffusive part is handled exactly in Fourier space. The nonlinear convective part is computed with an explicit fourth-order Runge-Kutta method with adaptive time-stepping, to ensure stability as the flow accelerates. As the flow decelerates, however, we keep the time-step δt at least 10 times smaller than the time interval Δt between two subsequent localized vortices. For simplicity, we set the time step in the Taylor approximation equal to the time step of the Runge-Kutta scheme. The value of the hyperviscosity, $\nu_H = 10^{-7}$, was found to guarantee numerical stability and effectively remove unresolved features on the 128×128 grid, which we used in all our calculations.

While we cannot claim that there is detailed numerical resolution for the smallest vortices in the computations, their effect on the large scale features of the flow nevertheless is negligible for the computations presented here. Comparisons of numerical solutions on different grids showed that bulk features of the flow, such as the energy or the L_2-error in velocity, hardly change if we further refine the underlying grid – see also [15].

Random forcing

The evolution of the dynamics is governed by the external forcing F and is chosen to mimic a random bombardment of the flow with smoothed small scale vortices,

$$F(x, y, t) = \sum_{j=1}^{\infty} \delta(t - t_j)\omega_r(\vec{x} - \vec{x}_j). \tag{36}$$

The smoothed small scale vortex is added at the random location $\vec{x}_j$ and has support in a disk of radius r_j,

$$\omega_r(\vec{x}) = A\left(1 - \frac{|\vec{x} - \vec{x}_j|^2}{r_j^2}\right)^2, \qquad |\vec{x} - \vec{x}_j| \leq r_j, \tag{37}$$

$$\omega_r(\vec{x}) = 0, \qquad |\vec{x} - \vec{x}_j| > r_j. \tag{38}$$

The random locations $\vec{x}_j$ are uniformly distributed inside Ω within a narrow margin away from the boundary of Ω. The radii r_j of the vortex patches vary randomly between $4\Delta x$ and $8\Delta x$, where $\Delta x = 2\pi/128$ is the mesh size. We approximate the temporal delta functions in (36) by the large constant value $1/\delta t$ over the time interval, $t_j \leq t \leq t_j + \delta t$, where δt is the current step size. In all calculations the amplitude $|A|$ of the added vortices remained constant for all time, yet we allow for a sign change of A. The value of A is either equal to one or to a percentage of the maximal vorticity of the initial flow configuration. Unless the forcing is identically zero, the time interval between two subsequent vortices remained constant and equal to $\Delta t = 0.1$ in all computations. Thus, during a numerical experiment up to $t = 1000$, the flow has been bombarded with $10,000$ smoothed point vortices, while the numerical integration has performed at least $100,000$ time steps. The required

increasingly smaller time steps at higher velocities remain the major obstacle to long-time numerical experiments at higher Reynolds numbers. In contrast, the crude closure algorithm is not affected by the Reynolds number; in fact, it tends to perform better at higher Reynolds number.

Random topography

In Sections 3, 4, and 5, we shall use the random topography,

$$h(x,y) = H \sum_{1 \le |\vec{k}| \le 5} h_{\vec{k}} \, e^{i\,\vec{k}\cdot\vec{x}}, \qquad \vec{x} = (x,y), \quad \vec{k} = (k_1, k_2), \tag{39}$$

where

$$h_{\vec{k}} = \frac{H_0}{|\vec{k}|^2} \, e^{i\theta_{\vec{k}}}, \qquad h_{-\vec{k}} = h_{\vec{k}}^*. \tag{40}$$

Here the constant H_0 normalizes the coefficients $h_{\vec{k}}$ to ensure that the maximal total height is H, and the random phase shifts $\theta_{\vec{k}}$ are chosen from a uniform distribution in $[0, 2\pi)$. Due to the decay of the Fourier coefficients like $|\vec{k}|^{-2}$, the topography is smooth. A medium-sized topography corresponds to $H = 1$, whereas $H = 10$ corresponds to a rather tall topography. For random topography in the channel or basin, we impose the appropriate symmetry condition in (39) to ensure that $h(x,y)$ vanishes on the boundary of Ω. The random layered topography in Section 6 is obtained through a one-dimensional expansion in Sine-functions analogous to (39).

3 Topographic flows in a basin

We shall now submit the crude closure dynamics presented in Section 2 for barotropic flow over topography to a series of successively more stringent tests. The underlying random topography is chosen according to (39) with $H = 1$; it is shown in Figure 1 and respects the symmetry imposed by the basin geometry.

3.1 Decaying flow

We begin with a purely decaying flow situation and thus set $F = 0$ in (1). The initial flow configuration is set to a perturbed steady state with $\mu = -1.5$. The perturbation consists of sixteen random vortices, eight rotating clockwise and eight rotating counter-clockwise, with fixed amplitude equal to 50% of the maximal initial vorticity, $|\omega|_{\max} \simeq 3.5$. The Ekman drag coefficient is set to $d = 0$ and the viscosity to $\nu = 0.01$, which results in a Reynolds number $Re = 400$. Figure 2 depicts selected snapshots of the potential vorticity at times $t = 0, 1, 5, 20, 58, 80$. The small-scale vortices, entrained by the background flow, interact and merge rapidly to form a large vortex, which spreads to the boundary of the domain. These initial stages clearly parallel the long-time behavior of solutions to the 2–D Navier-Stokes equations (without topography) predicted by the theory of selective decay (see Majda and Holen [14]). Yet, as the flow evolves further in time, small vortex structures begin to emerge and eventually correlate with the topography.

Figure 3 provides the explanation to this peculiar long-time behavior of the flow. During the initial phase of decay the energy, the enstrophy, and the maximal potential vorticity consistently decrease with time while the circulation clearly remains negative. The evolution of the flow is dictated by the relative vorticity, ω, which dominates the potential vorticity $q = \omega + h$. Here topography plays a minor role and the flow evolution bears resemblance to the Taylor vortex predicted by selective decay for flow without topography [14]. However, as the relative vorticity decreases further, the circulation changes sign while both $\mathcal{E}$ and $|q|_{\max}$ begin to increase again. During this second phase of pure decay the topography dominates the dynamics of the potential vorticity. Eventually ω approaches zero which results in the strong correlation of q and h. This numerical solution exhibits some of the behavior noted in the classical study from [19].

In Figure 3 we compare the exact (numerical) solution with the approximate solutions defined by the statistical states. The middle two frames show the relative errors in the macrostates q^*, obtained by matching the value of the energy from the exact solution. Both the relative errors in $\vec{v}$ and in q lie below 10% until $t = 50$. At later times the relative errors increase but this is somewhat misleading since these flows have nearly zero energy. As expected, the relative error in q is larger than the relative error in $\vec{v}$.

Next, we explore the accuracy of the approximate solution $\bar{q}$ determined by the crude closure algorithm. In the upper left frame of Figure 3, the exact energy, E, and the approximate energy, $\bar{E}$, are shown. The two curves can barely be distinguished from each other, which demonstrates that the crude closure predicts the evolution of the energy remarkably well. We recall that the crude closure dynamics evolve independently and without knowledge of the numerical solution, once the energy of the initial state has been matched at $t = 0$. Since the statistical states are completely determined by $\bar{E}$, which essentially coincides with the exact energy E, the relative L_2-errors of the macrostates obtained via the crude closure dynamics also coincide with those obtained through direct matching. Thus, the resolved flow from the numerical solution provides little extra information for bulk features of the flow as compared with the crude closure algorithm.

3.2 Spin-up of large vortex

Here we consider a numerical experiment radically different from the previous one. Initially at rest, the flow is bombarded with localized vortices of like negative sign and constant amplitude $|A| = 1$. What is the statistical quasi-equilibrium state for large times with damping and driving?

In our first calculation we set $\nu = 0.01$, so that statistical equilibrium was reached around $t \simeq 500$, with a final Reynolds number close to 2200. Since the macrostates are not defined for zero energy ($E \to 0$ implies $\mu \to \infty$), we add a single random vortex to quiescent flow and use the corresponding energy to initialize the crude closure algorithm. Then the initial energy at $t = 0$ is small but positive, typically $E(0) = O(10^{-4})$.

Figure 4 depicts snapshots of the potential vorticity during initial and later stages in the computation, $t = 0, 1, 5, 10, 50, 2000$. At $t = 0$ the small vortex added

ab initio is clearly visible against the contour lines of the topography. The initial stages of the flow are strongly perturbed and incoherent, yet with time a vortical super-structure emerges from the turbulent flow with the vorticity concentrated in the center of the basin. In Figure 5 we see the large increase in energy, as the flow accelerates due to the incessant bombardment with small vortices up to $t = 2000$ – until that time 20,000 random vortices have been added. The circulation, negative since the flow rotates clockwise, decreases below -5. The two middle frames in Figure 5 display the errors in velocity and vorticity using the macrostates obtained by matching the energy of the exact solution. The relative errors, as expected, are quite large during the initial stages, but rapidly decrease and reach remarkably small values considering the crude closure being utilized: 2% for the velocity and 5% for the vorticity. Simultaneously, the correlation is very poor during initial stages but drops down significantly to values around 0.002 for larger time, while Λ_ω and Λ_q stabilize about moderate values, indicative of prevailing large scale structures and smooth flow features. The lower two frames of Figure 5, which focus on the initial stages of the flow, emphasize the incoherent initial flow stages governed by rough small scale interaction with poor correlation and high values of Λ_ω and Λ_q. Both Λ_ω and Λ_q rapidly reach values close to $-\lambda_1 = 2$.

At this stage we address a remaining crucial issue: is the crude dynamics algorithm able to bridge over the initial chaotic stages of the flow and predict the bulk features of the emerging super-vortex ? Surprisingly, the answer to this question is yes. Indeed in the middle two frames in Figure 5, the errors in velocity and vorticity, obtained with the crude closure algorithm are barely larger than those obtained by the simple matching procedure.

How much do the results depend on the size of the topography ? To answer this question we magnify the topography by a factor ten and repeat the previous numerical experiment, with $H = 10$ in (39). Again, under the constant bombardment with random like signed vortices, the flow undergoes a transient incoherent state masked by the dominating topography, while q remains strongly correlated to h. However, as the flow picks up speed and ω decreases further, the enstrophy reaches zero by $t = 38$ and the correlation of q and ψ becomes very poor. At this stage, topography and relative vorticity compete until the potential vorticity rearranges itself and a large vortex emerges to fill the basin – see Figure 6. Beyond the initial perturbed flow configurations, the flow correlates extremely well with the statistical states. In the middle two frames of Figure 7, we see the remarkable performance of the crude closure algorithm, with relative errors again about 2% for the velocity and 5% for the vorticity. Until $t = 100$ the relative errors in velocity of the macrostates obtained by matching the exact energy lie slightly below those predicted by the crude closure; however, at later times the crude closure recovers the same level of accuracy. We refrain from showing long time simulations as the significant differences from the previous case with smaller topography occur only during the initial stages of the simulation.

The wide range of possible parameter settings is well represented by the above two situations of medium sized and tall topography. If one increases the topography even further without increasing the forcing, the flow eventually lingers in a low energy state governed by the underlying topography. As a consequence, the value of

13

Λ_q remains large and the performance of the crude closure is poor due to the small amount of mixing. In contrast, smaller topography leads to behavior increasingly similar to that without topography, where the crude closure performs well – see ref. [15]. Higher Reynolds number flows yield similar results but the flows do not reach a statistical equilibrium until much larger times. We omit showing results with combined Newtonian viscosity and Ekman drag, as they are quite similar.

3.3 Forcing by alternating opposite signed vortices

Finally, we attempt to explore the limits of the statistical theory and set $\nu = 0$. The hyperviscosity remains active with $\nu_H = 10^{-7}$. By strongly perturbing the flow with random localized vortices of alternating opposite sign, we attempt to force it out of the statistical state and test the performance of the crude closure algorithm. Figure 8 displays snapshots of the potential vorticity at times $t = 0, 400, 800, 1600$. The initial flow configuration corresponds to the steady state with $\mu = -1$. Since the initial energy is not zero in this case, the crude closure is well-defined from the start and no small vortex needs to be added at $t = 0$. In contrast to the behavior during pure decay or build-up from zero, the contour lines of the potential vorticity rapidly concentrate in the center of Ω. Then, by $t = 800$, a large secondary vortex structure appears along the boundary of Ω as the main vortex shifts away from the center and wanders about the basin. As to be expected under such harsh conditions, the statistical states correlate rather poorly with the evolving flow and lead to errors around 40% in the velocity. In Figure 9 the strong variations in the maximal velocity and the constant increase of both Λ_ω and Λ_q indicate the increasingly strong activity in the small scales. Surprisingly, the crude closure is able to track bulk features of the flow, such as the energy, quite accurately and for all time, in spite of poor correlation and large relative errors in the velocity. Note that the evolution of the energy predicted by the crude closure departs only slightly from that of the exact energy around $t = 1200$ and that the two curves meet again around $t = 1500$. Although increasing ν always leads to smoother flows and smaller relative errors, the net input of energy of the alternating small scale forcing remains marginal and as a consequence the flow rapidly decays to zero.

4 Topographic flows in a channel

With the clear evidence presented in the previous section for the merit of the crude closure dynamics in damped and driven flows in a basin, it is natural to ask whether a similar behavior can be expected in a different geometry. In this section we choose Ω to be a channel and set h again to be a random topography with $H = 1$, sampled according to the prescription in (39) and shown in Figure 10. We remark that due to our initial assumption that the integrals of ψ and h vanish, neither our numerical simulation nor the family of statistical states of the energy-enstrophy theory allow for the most basic pattern in channel flow, namely constant uniform flow.

4.1   Spin-up from zero

As in the previous section we set the viscosity to $\nu = 0.01$ and bombard the flow, initially at rest, with localized vortices of like negative sign and constant amplitude $|A| = 1$. In Figure 11 we display snapshots of the potential vorticity during initial and later stages in the simulation, $t = 0, 1, 5, 10, 50, 2000$. Again at $t = 0$ the single small vortex added ab initio is clearly visible against the contour lines of the topography. Although initial stages of the flow are strongly perturbed, the flow rapidly develops two large vortices in opposite direction, which correlate with the dominant topographic features. Under the incessant bombardment with small vortices, the flow accelerates further and changes its topology as the counter-clockwise vortex in the center is torn apart and a large scale shear flow emerges around $t = 50$. This shear flow configuration remains stable to small scale perturbation until $t = 500$, when the flow reaches a quasi-equilibrium state.

Despite the dramatic change in the flow topology, shown in Figure 11, the crude closure rapidly bridges over the initial turbulent stages and predicts the emergence of a shear flow with the same accuracy as for flow in the basin, with relative errors in the velocity below 2% and in the vorticity around 4%. Final values of the velocity lie around $|\vec{v}| = 8.5$, which corresponds approximately to a Reynolds number of $Re = 5400$. The lower two frames in Figure 12 display the correlation and both Λ_ω and Λ_q, again during the initial stages of the simulation until $t = 50$. We note the very poor correlation of the flow with the macrostates up to $t = 10$, paralleled by very large values in Λ_ω and Λ_q, which demonstrate the strong vortical activity in the small scales. As the energy cascades from smaller to larger scales, the ratio of enstrophy to energy diminishes and coherent structures appear in the evolving flow, which eventually stabilizes into a large scale shear flow configuration.

4.2   Forcing by alternating opposite signed vortices

Again we attempt to push the crude closure to the limits of statistical theory and set $\nu = 0$. The initial flow configuration corresponds to the macrostate defined by $\mu = -1/2$. By strongly perturbing the flow with random vortices of alternating opposite sign, we attempt to push the flow away from statistical equilibrium. The small smoothed vortices all have constant amplitude equal to 10% of the initial maximal relative vorticity. Figure 13 displays snapshots of the potential vorticity at times $t = 0, 400, 800, 2000$. Under the incessant bombardment with small smoothed vortices, a counter-clockwise vortex concentrates in the center of the channel around $t = 400$, to be destroyed again by $t = 2000$. By that time the contour lines of the dominant vortex have lost their initially smooth character and appear tightly packed.

The rough nature of the flow is apparent from the slow but steady increase in Λ_ω and Λ_q, shown in Figure 14, while the maximal potential vorticity triples over the entire simulation. The increase in Λ_q demonstrates the absence of an inverse energy cascade. Indeed the small vortices added by the random forcing accumulate in the smaller scales of the flow and result in a fivefold increase in the enstrophy, while we observe little change in the energy. Despite the poor correlation with statistical states, with relative errors in the velocity as high as 30%, the crude closure algorithm tracks the evolution of the energy within a few percent.

5 Topographic flows in periodic geometry

Unlike the two previous geometries, periodic geometry requires the circulation to vanish for all time. Thus any flow configuration must consist equally of regions with positive and with negative vorticity, and it is not possible to build a large scale flow through bombardment with random like signed vortices. To enforce the zero circulation constraint, we shall add *two random vortices of identical strength but opposite sign* at each $\bar{t}$. Hence the set-up for the numerical experiments in this section with $\nu = 0$ is comparable to that in sections 3.3 and 4.2. The underlying random topography, shown in Figure 15, is defined by (39) with $H = 1$.

We begin with a low energy simulation and set the initial flow to the statistical steady state defined by $\mu = -1/2$. The amplitude of the small scale forcing is set to 10% of the initial maximal relative vorticity, $|\omega|_{\max} \approx 1.5$, or equivalently to 30% of the initial maximal potential vorticity, $|q|_{\max} = 0.51$. As a result of the strong random forcing – recall that two vortices of opposite sign are added at each $\bar{t}$ – and the absence of viscosity, the contour lines of q in Figure 16 appear very perturbed at later times. Both Λ_q and Λ_ω remain essentially constant during the entire numerical experiment, while we observe a slight decrease in energy at later times. The crude closure tracks the energy quite accurately, while the strongly perturbed flow features yields relative errors in velocity between 10% and 20%.

Next, we repeat the same numerical experiment but set the initial flow to the statistical state defined by $\mu = 5$. Here the energy is about 100 times smaller than in the previous case. In addition, unlike in the previous simulation, the maximal relative vorticity, $|\omega|_{\max} \approx 0.35$, is smaller than the maximal potential vorticity, $|q|_{\max} \approx 0.66$ so we have very weak initial flow dominated by topography. As a consequence, the amplitude of the forcing, still set to 10% of $|\omega|_{\max}$, is only about 5% of $|q|_{\max}$, which results in rather smooth contours in q at later times, shown in Figure 17. The variations in the evolution of $|q|_{\max}$ are also smaller than in the previous case. The large values in Λ_q, about fifteen times larger than in the previous case, indicate the enhanced role of small scale topographic features versus that of random forcing. As anticipated from the larger values of Λ_q, the performance of the crude closure is worse and the algorithm is unable to follow accurately the evolution of the energy.

6 Layered two-mode topography in the channel

In this last section we restrict ourselves to the following layered two-mode topography in the channel,

$$h(x, y) = H \left(\frac{\sin y}{2} + \sin(2y) \right). \tag{41}$$

This peculiar topography differs from previous random topography (39) in two ways: first, it is layered, that is $h = h(y)$; second, in contrast to the smooth decay of Fourier coefficients of h in (39), here the second Fourier mode clearly dominates over the first mode. In general, the performance of the crude closure for flow over layered topography hardly differs from that over random topography studied in Section 5.

For instance, if we set $\nu = 0.01$ and $H = 1$, as in Section 5, and spin up the flow from zero with like signed vortices of amplitude $|A| = 1$, both random (layered) topography, defined by (39) with $h = h(y)$, and the above two-mode topography lead to similar results. Indeed in both cases the crude closure predicts the eventual final state of a shear flow, with relative errors in velocity below 10% for flow over two-mode topography and around 3% for flow over random topography. We refrain from showing these results, which simply corroborate the findings from our previous study. Instead, we shall devise special flow situations over two-mode topography at low energy, which illustrate the shortcomings of the crude closure based on the energy-enstrophy theory. Although the flows considered in this section are somewhat atypical and contrived, they demonstrate the potential benefit to be gained from the use of more sophisticated statistical theories, such as the Langevin theory discussed in Section 2.3.

6.1 Failure of the crude closure

We now describe a special low energy dynamic transition of the flow over layered two-mode topography, which the crude closure based on the energy-enstrophy theory is unable to predict. We let the topography be given by (41) with $H = 1$ and set the initial conditions to the steady state defined by (15) with $\mu = -0.5$. Since the topography is layered and the mean-field equation is linear, the initial condition as well as any other steady state is necessarily layered. Hence the initial flow, shown in Figure 18, is a shear flow with slightly negative circulation. We set the viscosity to $\nu = 0.01$ and choose the amplitude of the forcing $|F| = 0.15$, about 10% of the initial maximal vorticity, so that the flow remains in a low energy state, $E = O(0.1)$. Under the constant bombardment with small clockwise vortices, the energy decays until $t = 20$ but then increases to reach a steady value around 0.2, while a clockwise vortex emerges in the upper half of the channel. Although the crude closure predicts the initial decrease in energy, it fails to predict the subsequent increase. The crude closure with only two layered modes attempts to approximate the exact solution with a strong emerging large scale vortex. During this dynamic transition from a layered to a vortical flow configuration, we observe a large, fifty-fold increase in Λ_q. Since the family of steady states is restricted to zonal shear flows, the crude closure cannot accommodate the emerging vortex. A possible remedy may be the use of crude closure based on more sophisticated statistical theories, such as the Langevin theory discussed in Section 2.3, which yield a richer family of statistical states not restricted to zonal shear flows.

6.2 Langevin statistical theories

To demonstrate the potential benefit from using more complex statistical theories, we choose a special situation for which the mean-field potential vorticity, q^*, of the Langevin statistical theory is not a zonal but instead a vortical flow. Again we set h to the layered two-mode topography in (41), but with smaller amplitude $H = 0.1$. The initial flow configuration is set to the entropy maximizer, q^*, which results from the Langevin theory for the special parameter choice $E = 0.28$, $\Gamma = -0.34$,

$Q_+ = 0.48$, and $Q_- = -1.67$ (see Section 2.4). It consists of a large vortex rotating clockwise, with a tight boundary; it is shown in Figure 19. Both the forcing and the dissipation are identical to the previous case, $|F| = 0.15$ and $\nu = 0.01$. Under the constant bombardment with like signed, small, clockwise vortices, a background shear rapidly appears which tears apart the initial vortex. By $t = 100$ the vortex has completely disintegrated and the flow remains in a shear flow configuration for all time. Despite the inability of the energy-enstrophy theory to accommodate the initial vortex, the crude closure easily predicts the increase and long term evolution of the energy as the flow stabilizes in a shear flow configuration, with relative errors in the velocity around 5%. Both Λ_ω and Λ_q rapidly reach their final values close to one.

Finally, we consider the same initial flow configuration but with $\nu = 0$ and bombard the flow with alternating opposite signed vortices of amplitude equal to 5% of the maximal initial vorticity. Here the flow remains in a vortical configuration over the entire time interval until $t = 1000$. The crude closure predicts the evolution of the energy without difficulty, despite relative errors in the velocity around 50% due to the inability of the energy-enstrophy theory to accommodate a vortex over layered topography. The vortex shifts about the channel, as shown in the top left frame of Figure 20. Moreover, its overall appearance evolves as its contours become smoother and stretched out in the zonal direction. We now wish to check the consistency of the Langevin statistical theory. To do so, we wait for the flow to regain the center of the channel, around $t = 670$. Then with the current values of the time dependent flow $E = 0.30$, $\Gamma = -0.48$, $Q_+ = 0.21$, and $Q_- = -2.31$, we compute the entropy maximizer of the Langevin statistical theory. The corresponding mean-field potential vorticity, q^*, is shown in the lower right frame of Figure 20 and compares favorably with the flow at $t = 670$, shown above it. In particular we note how the contours of q^* are also smooth and slightly stretched in the zonal direction. The relative error in potential vorticity is 19%, a clear improvement over the 70% relative error in the layered solution of the energy-enstrophy statistical theory. Although we have only verified the consistency of the Langevin theory, the crude closure algorithm could be extended to predict the evolution of the two additional parameters Q_+ and Q_-. This last example demonstrates the potential benefit resulting from the use of more complex statistical theories, such as the Langevin theory.

7   Concluding discussion

The equilibrium states of few constraint statistical theories have proved to be reasonably robust to small scale forcing in a variety of geometries and for a wide range of underlying topography. By using these equilibrium statistical states, we have devised a simple procedure, the crude closure algorithm, which predicts within a small error margin the general trend of large scale features of the flow as it evolves under intense, small scale forcing. Systematic comparison with the full numerical solution demonstrates that the one-parameter crude closure based on the energy-enstrophy theory generally tracks with high accuracy the evolution of bulk features of the flow, such as the energy. We have tested the crude closure for random and layered

topography in three types of geometry: the basin, the channel, and the periodic geometry. Typically the crude closure predicts the evolution of the energy within a few percent, while relative errors in velocity range from 5% to 10%. Exception to this situation, documented in sections 4, 5, and 6, occur when the energy-enstrophy ratio is large or increases rapidly in time. As demonstrated in section 6, more sophisticated statistical theories, as discussed in Section 2.2, can be used to enrich the family of statistical states by including additional conserved quantities and prior distributions. Then the resulting crude closure dynamics accommodate a wider range of flow regimes at the expense of a more complicated numerical procedure. The ratio of enstrophy to energy, Λ_q, has proved a reliable indicator for the performance of the crude closure, with improved performance at lower values. Large values of Λ_q indicate little if no inverse energy cascade and as a result no emergence of large scale coherent structures. Although strongly perturbed flows often produce large relative errors in velocity, the crude closure algorithm is able to track the evolution of bulk features of the flow quite accurately, as long as Λ_q is not too big. Large values of Λ_q correspond either to flow where all the energy resides in the small scales or to creeping flow dominated by topography, where little mixing occurs. Furthermore, whenever the flow crosses a rough transition where Λ_q is large and the correlation poor, the crude closure is able to predict the general trend of bulk features and recover its original accuracy. However, examples of failure of the crude closure to track the energy accurately through regimes with large Λ_q are documented in sections 5 and 6.1.

Given the encouraging results presented in this paper involving crude dynamical closure modeling based on large scale statistical theory, it is important to point out some limitations of the approach. The most important limitation involves the requirement of strong mixing or ergodicity of the flow field. This issue was circumvented here through the use of simple geometry and small scale random forcing with an essentially uniform distribution of locations. For more realistic geophysical flows involving large scale forcing and the beta-effect, distinct mixing regions can emerge through a combination of these effects ([1, 23]). It is very interesting to devise crude dynamics based on statistical theories which can account for these new physical effects. The authors are currently pursuing these issues and will report on them elsewhere in the near future.

References

[1] Holloway G 1986, Eddies, waves, circulation and mixing: statistical geofluid mechanics, *Ann. Rev. Fluid Mech.* **18** 91–147

[2] McWilliams J C 1984, The emergence of isolated coherent vortices in turbulent flow, *J. Fluid Mech.* **146** 21–43

[3] Kraichnan R H 1975, Statistical dynamics of two-dimensional flow, *J. Fluid Mech.* **67** 155–175

[4] Salmon R, Holloway G and Henderschott M C 1976, The equilibrium statistical mechanics of simple quasi-geostrophic models, *J. Fluid Mech.* **75** 691–703

[5] Montgomery D and Joyce G 1974, Statistical mechanics of negative temperature states, *Phys. Fluids* **17** 1139–45

[6] Pointin Y B and Lundgren T S 1976, Statistical mechanics of two dimensional vortices in a bounded container, *Phys. Fluids* **10** 1459–70

[7] Kraichnan R H and Montgomery D 1980, Two-dimensional turbulence, *Rep. Prog. Phys.* **43** 548–619

[8] Caglioti E, Lions P L, Marchioro C and Pulvirenti M 1992, A special class of stationary flows for two-dimensional Euler equations: A statistical mechanics description, *Commun. Math. Phys.* **143** 501–25

[9] Miller J 1990, Statistical mechanics of Euler equations in two dimensions, *Phys. Rev. Lett.* **65** 2137–40

[10] Miller J, Weichman P B and Cross M C 1992, Statistical mechanics, Euler's equation, and Jupiter's red spot, *Phys. Rev. A* **45** 2328–59

[11] Robert R 1991, A maximum entropy principle for two-dimensional Euler equations, *J. Stat. Phys.* **65** 531–53

[12] Turkington B, Statistical equilibrium structures and coherent states in two-dimensional turbulence 1998, *Comm. Pure Appl. Math.*, in press

[13] DiBattista M T, Majda A J and Turkington B 1998, Prototype geophysical vortex structures via large-scale statistical theory, *Geoph. Astr. Fluid Dyn.*, submitted

[14] Majda A and Holen M 1997, Dissipation, topography, and statistical theories for large scale coherent structure, *Comm. Pure. Appl. Math.* **50** 1183–234

[15] Grote M J and Majda A J, Crude closure dynamics through large scale statistical theories, *Phys. Fluids* **9** 3431–42

[16] Holloway G and Eby M, Hybrid statistical mechanics – ocean circulation for efficient large scale modelling, *Proc. of Oceans '93 (Victoria, BC, Canada)* vol 1 (Piscataway, NJ: IEEE Order Dept.) p 323

[17] Holloway G 1992, Representing topographic stress for large-scale ocean models, *J. Phys. Oceanography* **22** 1033–46

[18] Carnevale G and Frederiksen J 1987, Nonlinear stability and statistical mechanics of flow over topography, *J. Fluid Mech.* **175** 157–81

[19] Bretherton F B and Haidvogel D B 1976, Two-dimensional turbulence above topography, *J. Fluid Mech.* **78** 129–54

[20] Turkington B and Whitaker N 1996, Statistical equilibrium computations of coherent structures in turbulent shear layers, *SIAM J. Sc. Comput.* **17** 1414–33

[21] Wang J and Vallis G 1994, Emergence of Fofonoff states in inviscid and viscous ocean circulation models, *J. Marine Res.* **52** 83–127

[22] Treguier A 1989, Topographically generated steady currents in barotropic turbulence, *Geoph. Astr. Fluid Dyn.* **47** 43–68

[23] Griffa A and Salmon R 1989, Wind-driven ocean circulation and equilibrium statistical mechanics, *J. Marine Research* **47** 457–92
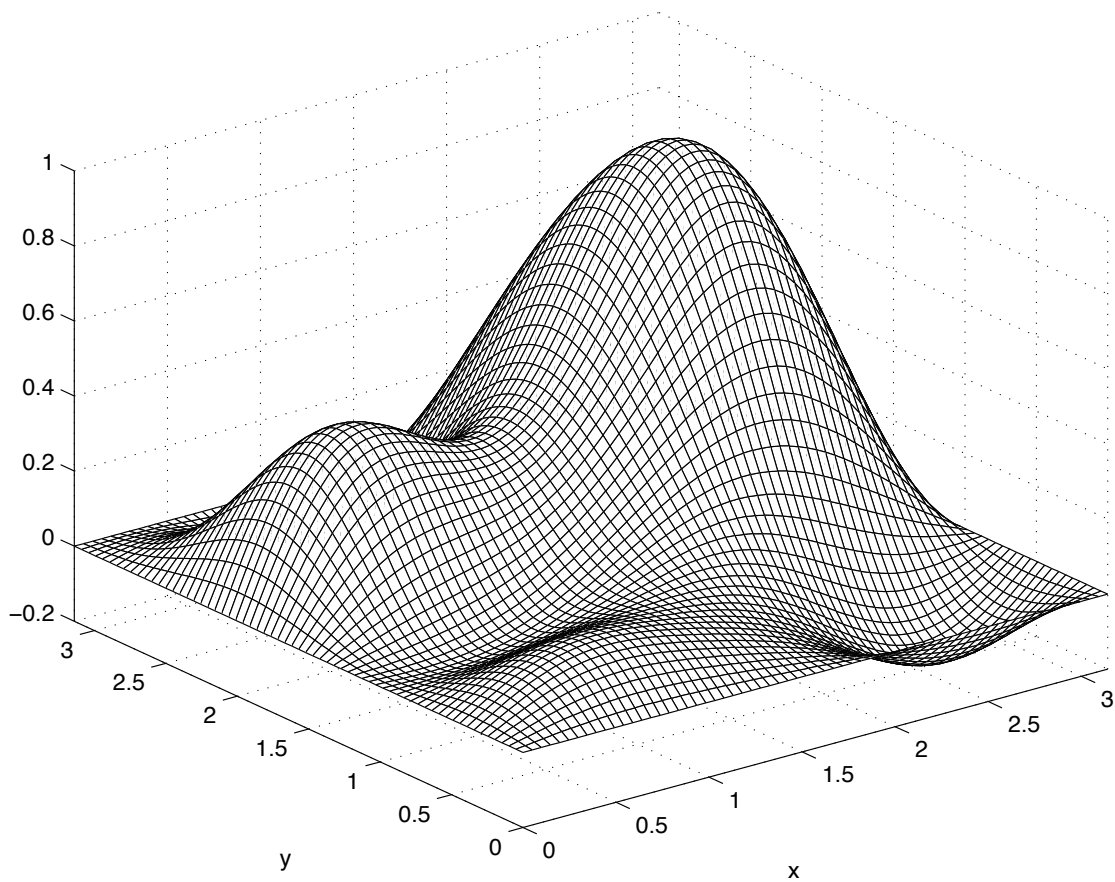
Figure 1: Random topography in the basin.
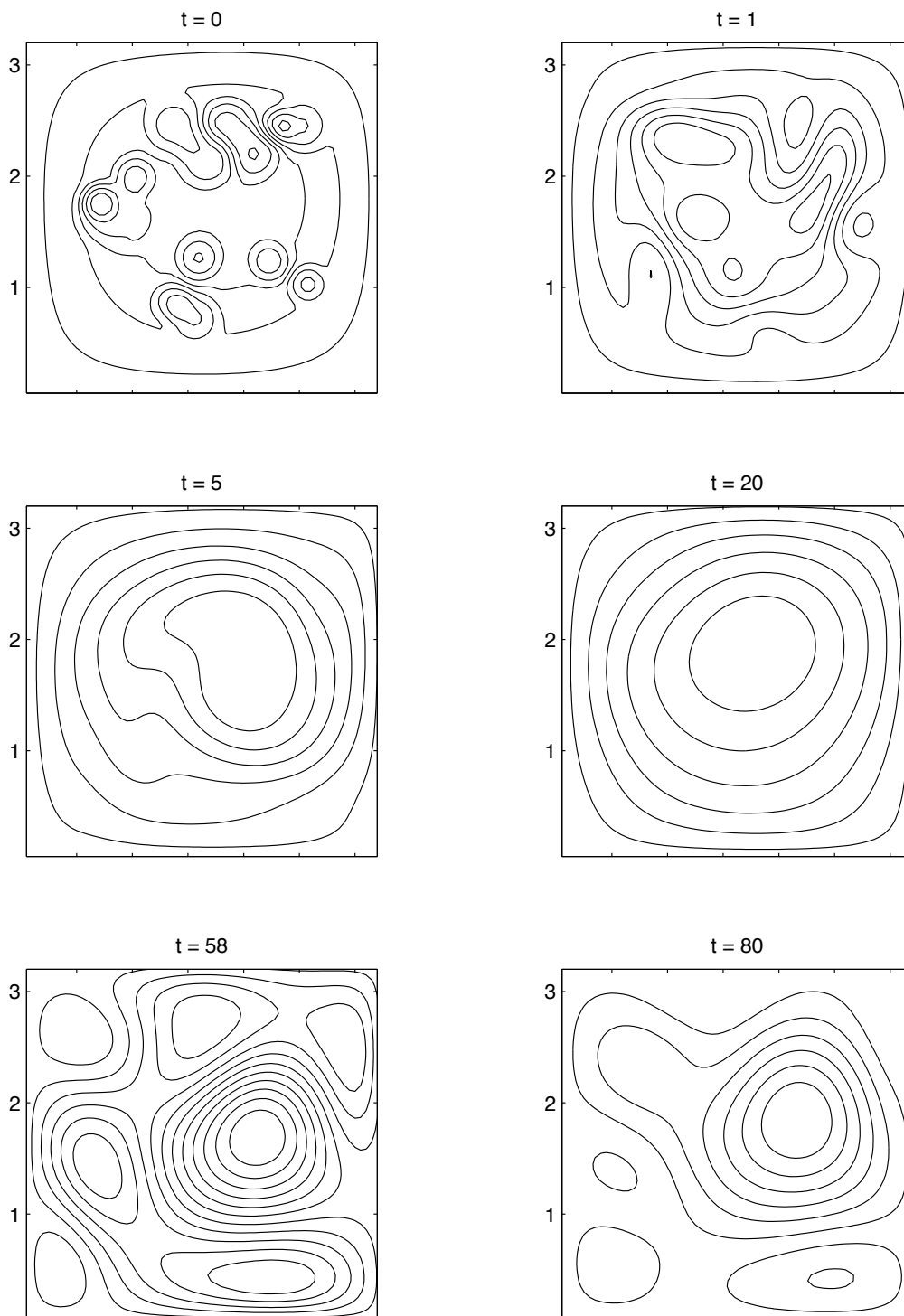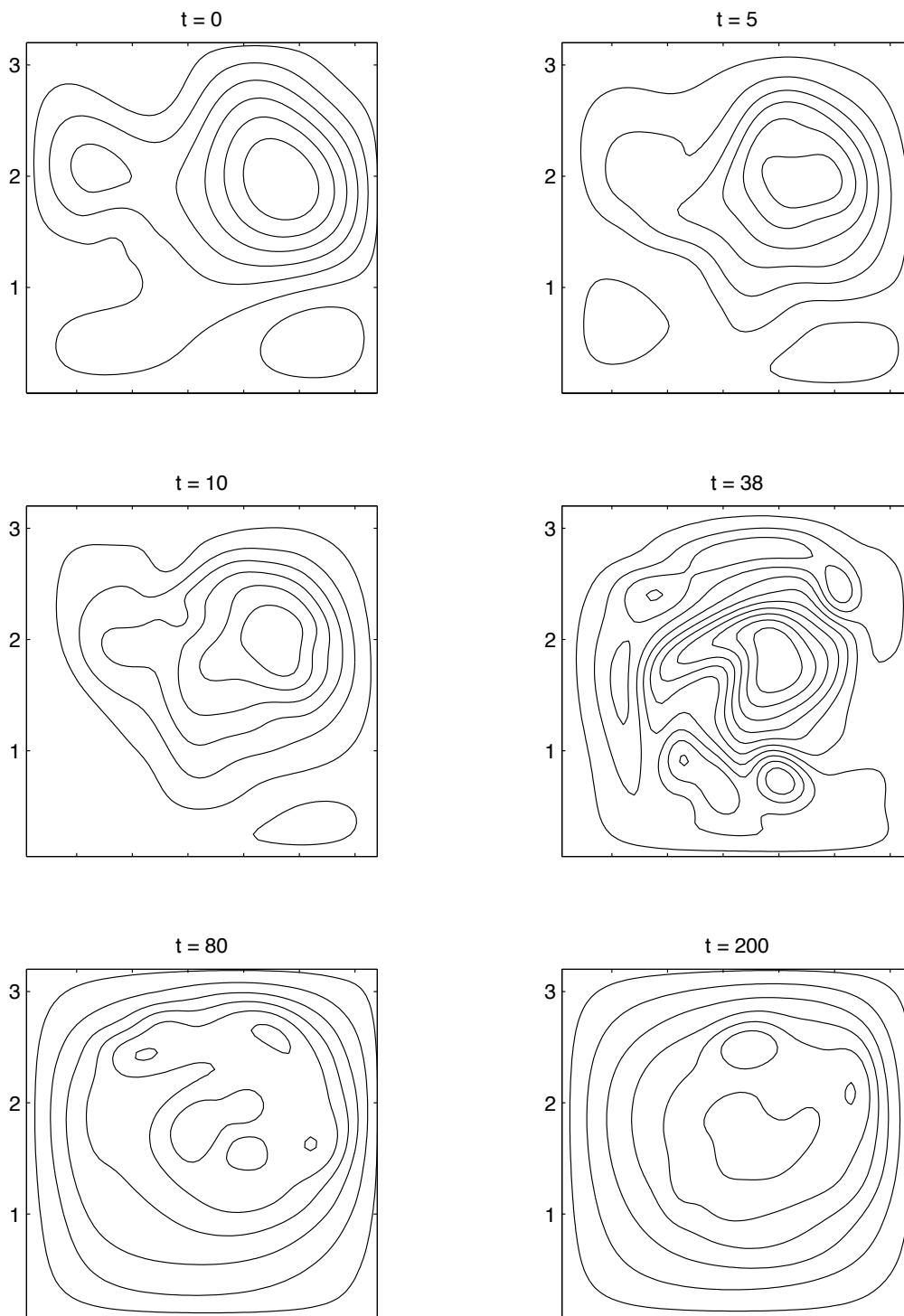
Figure 2: Snapshots of the potential vorticity at $t = 0, 1, 5, 30, 58, 80$ during pure decay in the basin, with $H = 1$ and $\nu = 0.01$.
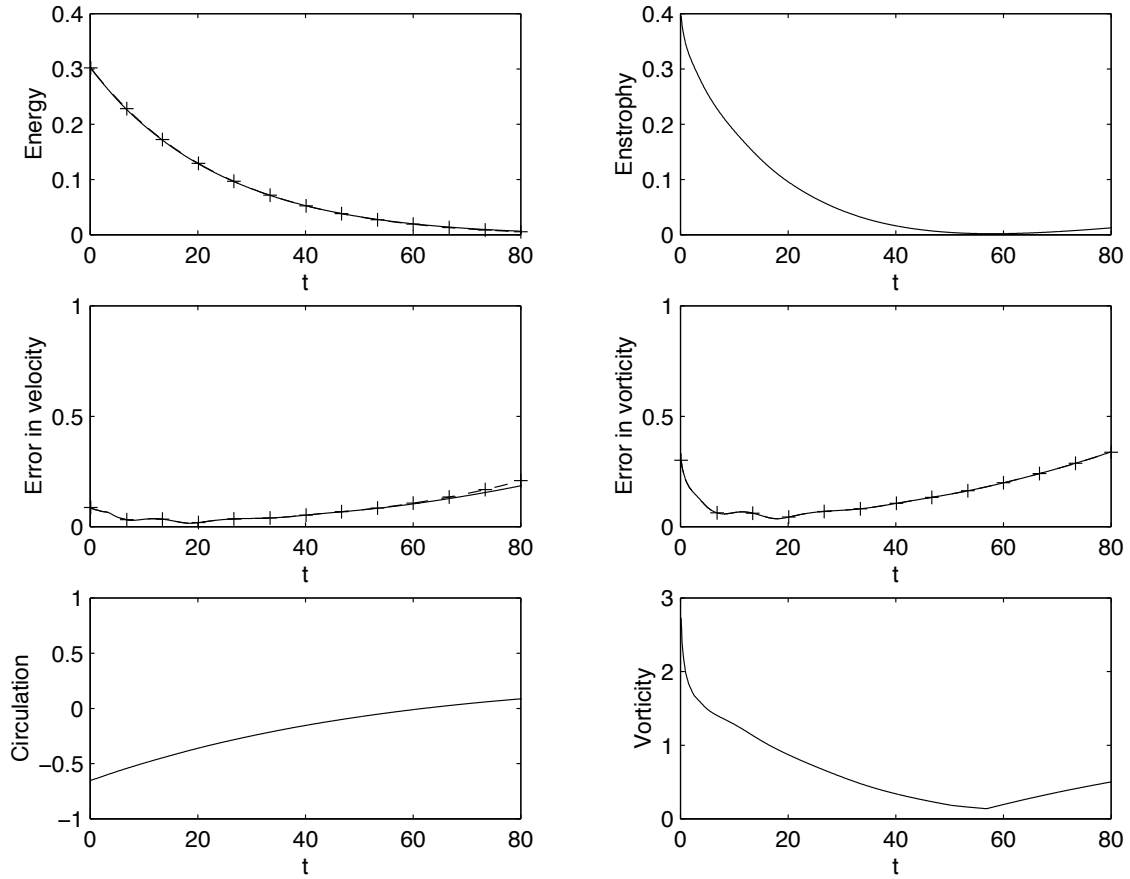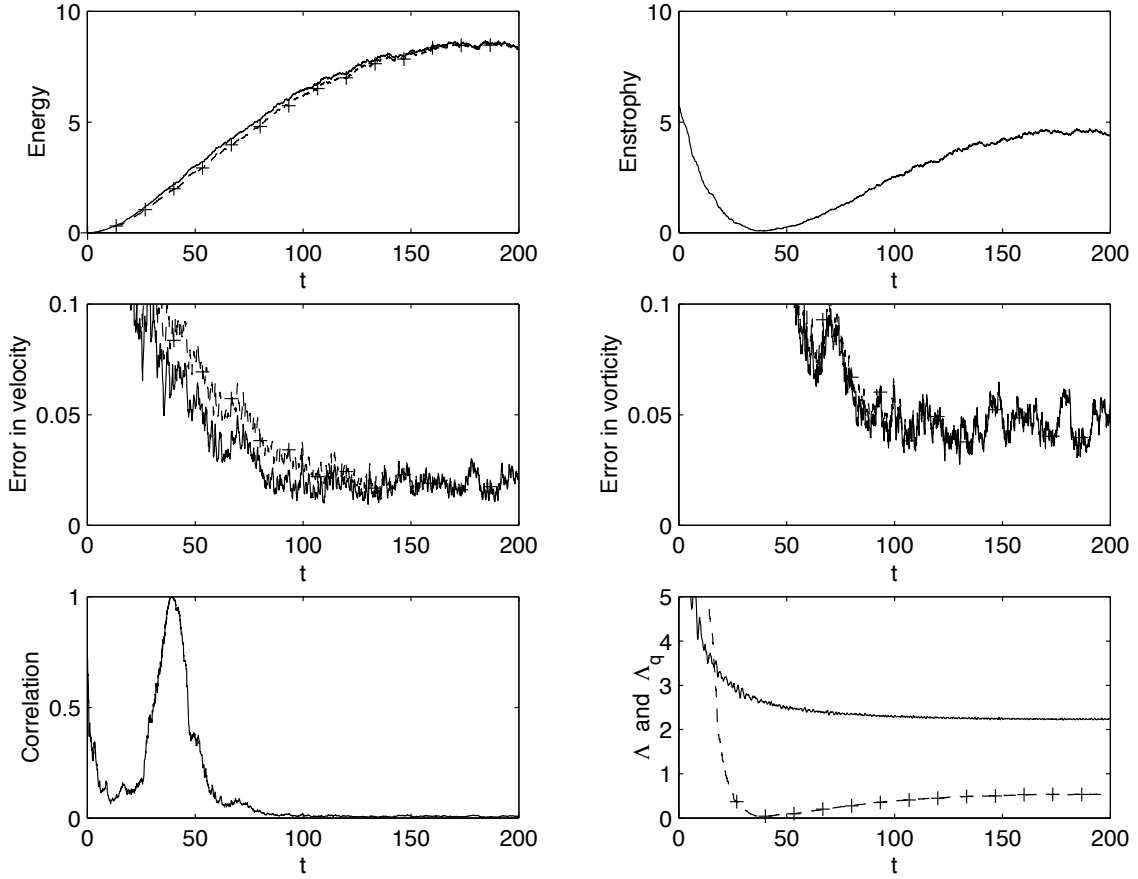
Figure 3: Comparison with crude closure dynamics during pure decay in the basin, with $H = 1$ and $\nu = 0.01$. Top left: energy E (plain) and predicted energy $\bar{E}$ $(+ - +)$; top right: enstrophy $\mathcal{E}$; middle left: relative errors in matched velocity $\mathrm{Err}(\vec{v}, \vec{v}^*)$ (plain) and predicted velocity $\mathrm{Err}(\vec{v}, \bar{\vec{v}})$ $(+ - +)$; middle right: relative errors in matched potential vorticity $\mathrm{Err}(q, q^*)$ (plain) and predicted potential vorticity $\mathrm{Err}(q, \bar{q})$ $(+-+)$; bottom left: circulation Γ; bottom right: potential vorticity q.
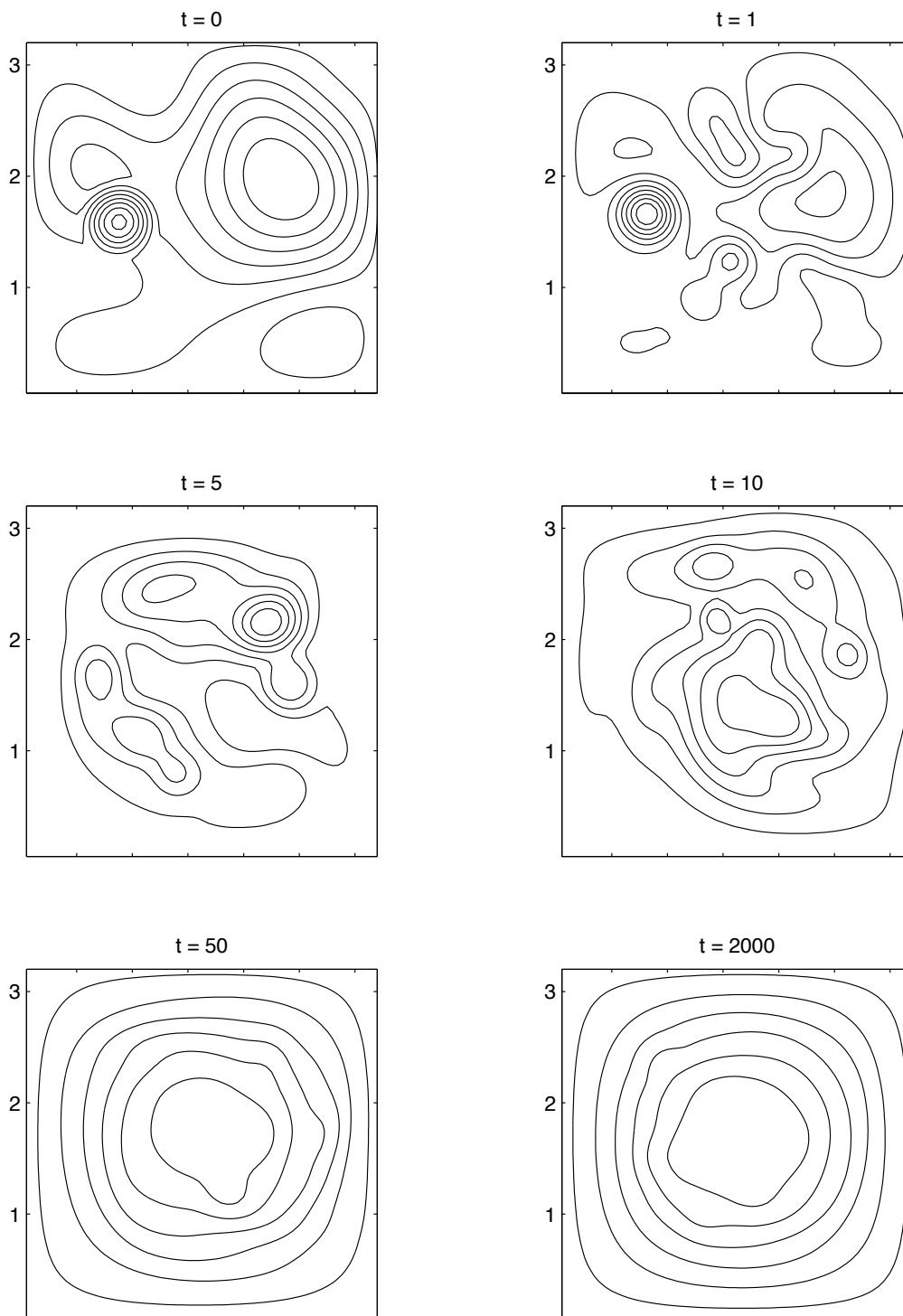
Figure 4: Snapshots of the potential vorticity at $t = 0, 1, 5, 10, 50, 2000$, during spin-up from zero in the basin, with $H = 1$ and $\nu = 0.01$.

25
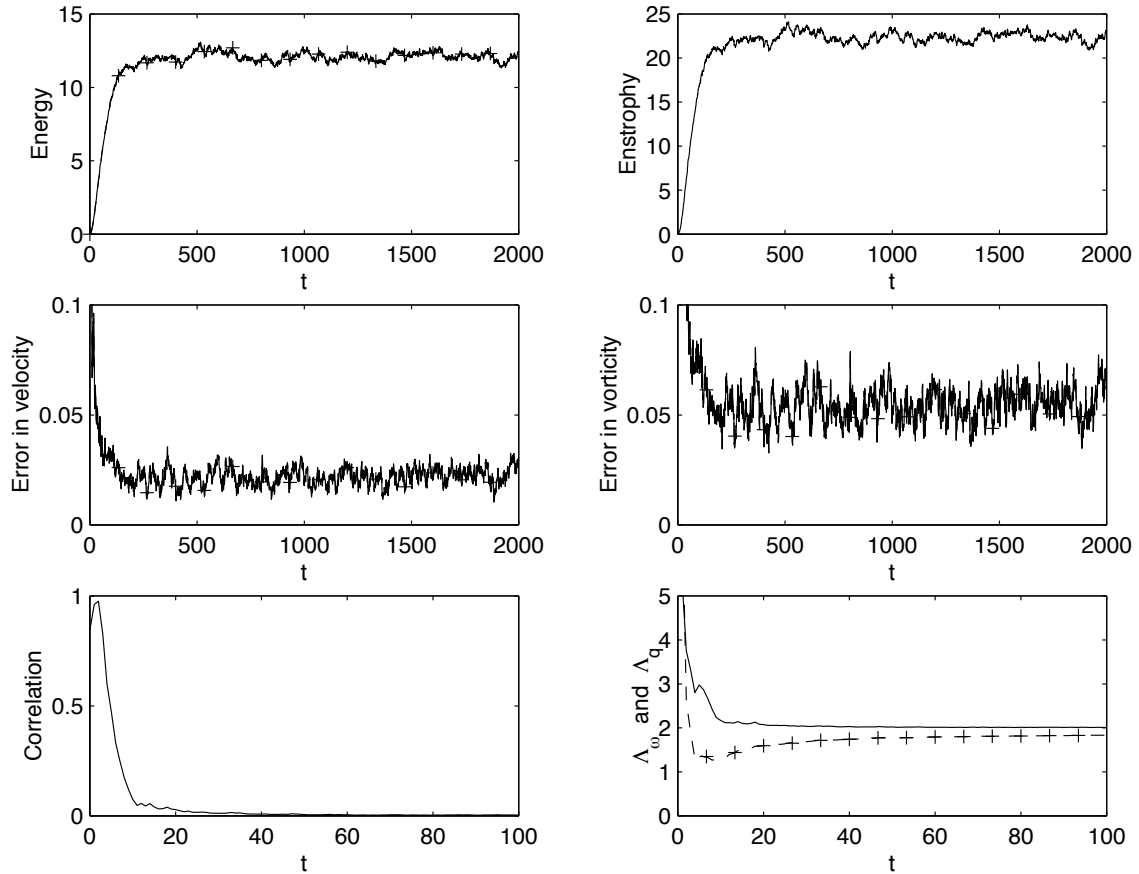
Figure 5: Comparison with crude closure dynamics during spin-up from zero in the basin, with $H = 1$ and $\nu = 0.01$. Top left: energy E (plain) and predicted energy $\bar{E}$ $(+ - +)$; top right: enstrophy $\mathcal{E}$; middle left: relative errors in matched velocity $\mathrm{Err}(\vec{v}, \vec{v}^*)$ (plain) and predicted velocity $\mathrm{Err}(\vec{v}, \bar{\vec{v}})$ $(+ - +)$; middle right: relative errors in matched potential vorticity $\mathrm{Err}(q, q^*)$ (plain) and predicted potential vorticity $\mathrm{Err}(q, \bar{q})$ $(+-+)$; bottom left: correlation $\mathrm{Corr}(q, \psi)$; bottom right: Λ_ω (plain) and Λ_q $(+ - +)$.
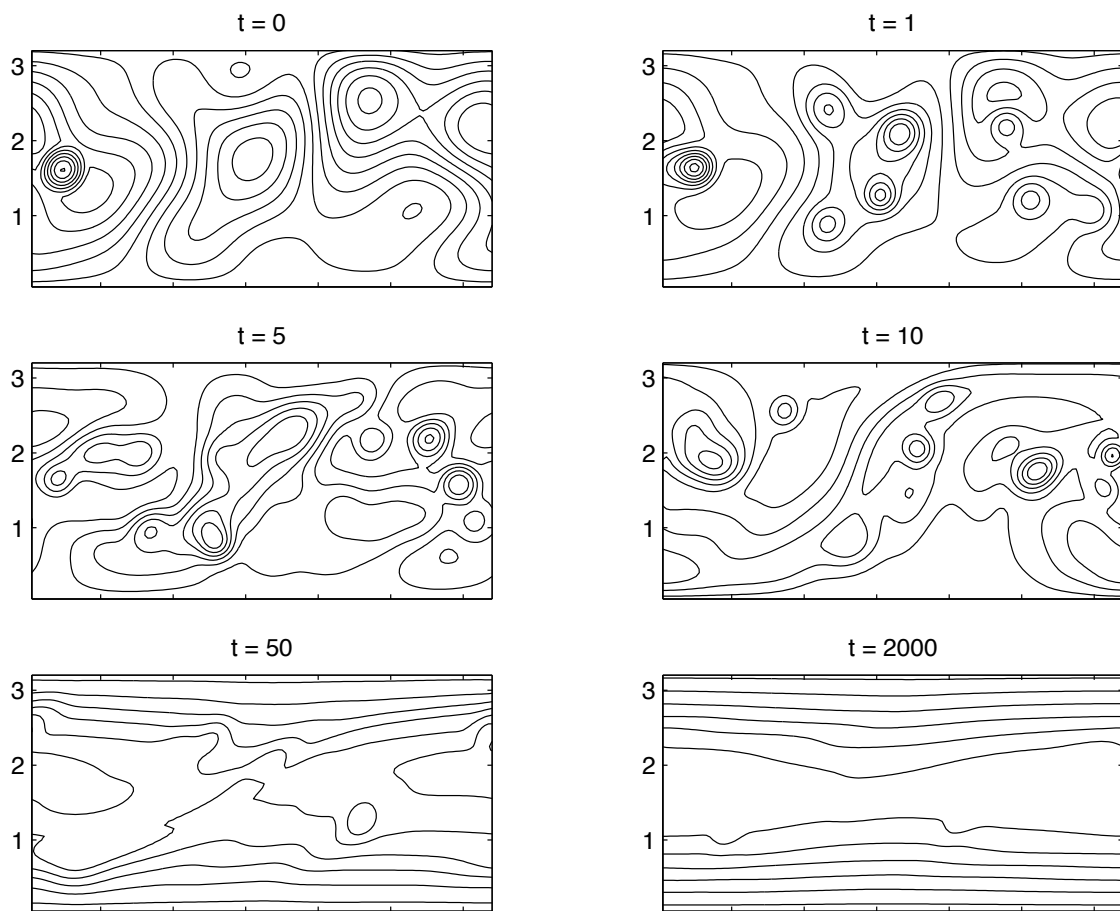
Figure 6: Snapshots of the potential vorticity at $t = 0, 5, 10, 38, 80, 200$, during spin-up from zero in the basin, with $H = 10$ and $\nu = 0.01$.
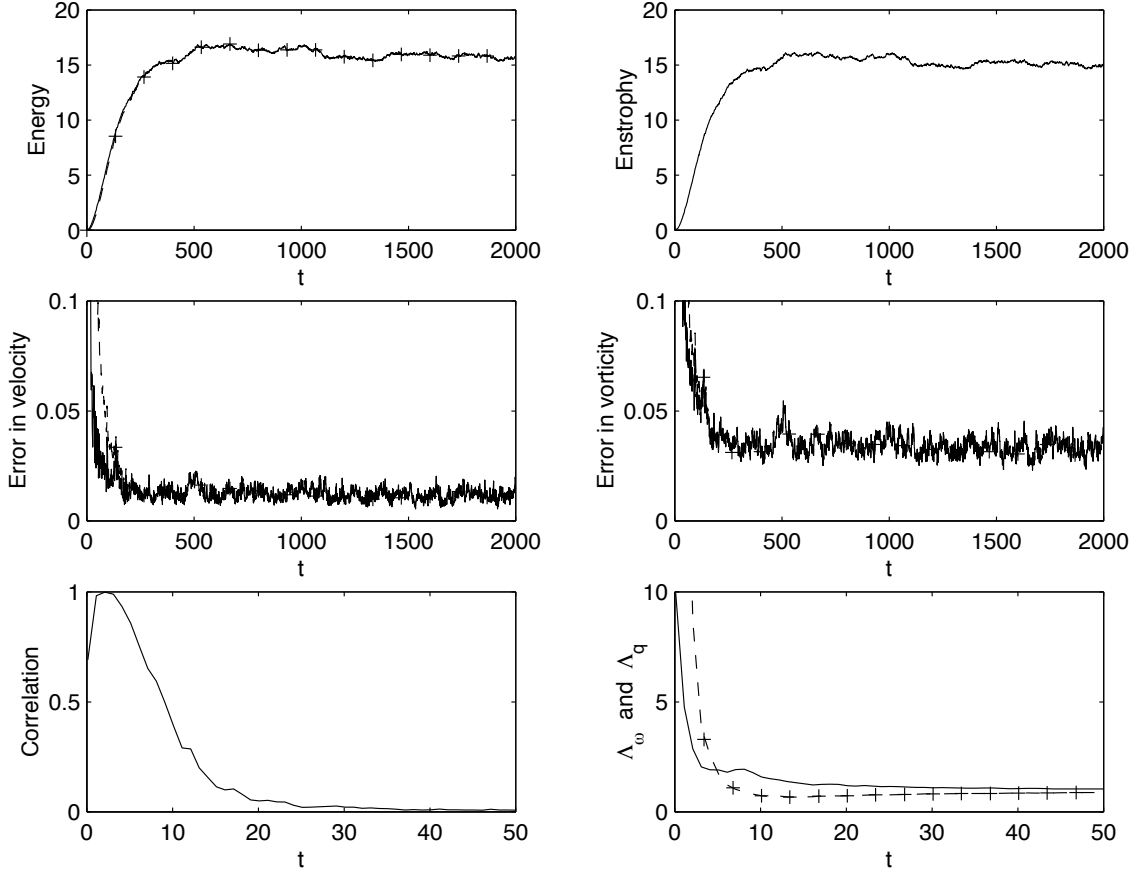
Figure 7: Comparison with crude closure dynamics during spin-up from zero in the basin, with $H = 10$ and $\nu = 0.01$. Top left: energy E (plain) and predicted energy $\bar{E}$ $(+ - +)$; top right: enstrophy $\mathcal{E}$; middle left: relative errors in matched velocity $\text{Err}(\vec{v}, \vec{v}^*)$ (plain) and predicted velocity $\text{Err}(\vec{v}, \bar{\vec{v}})$ $(+ - +)$; middle right: relative errors in matched potential vorticity $\text{Err}(q, q^*)$ (plain) and predicted potential vorticity $\text{Err}(q, \bar{q})$ $(+-+)$; bottom left: correlation $\text{Corr}(q, \psi)$; bottom right: Λ_ω (plain) and Λ_q $(+ - +)$.
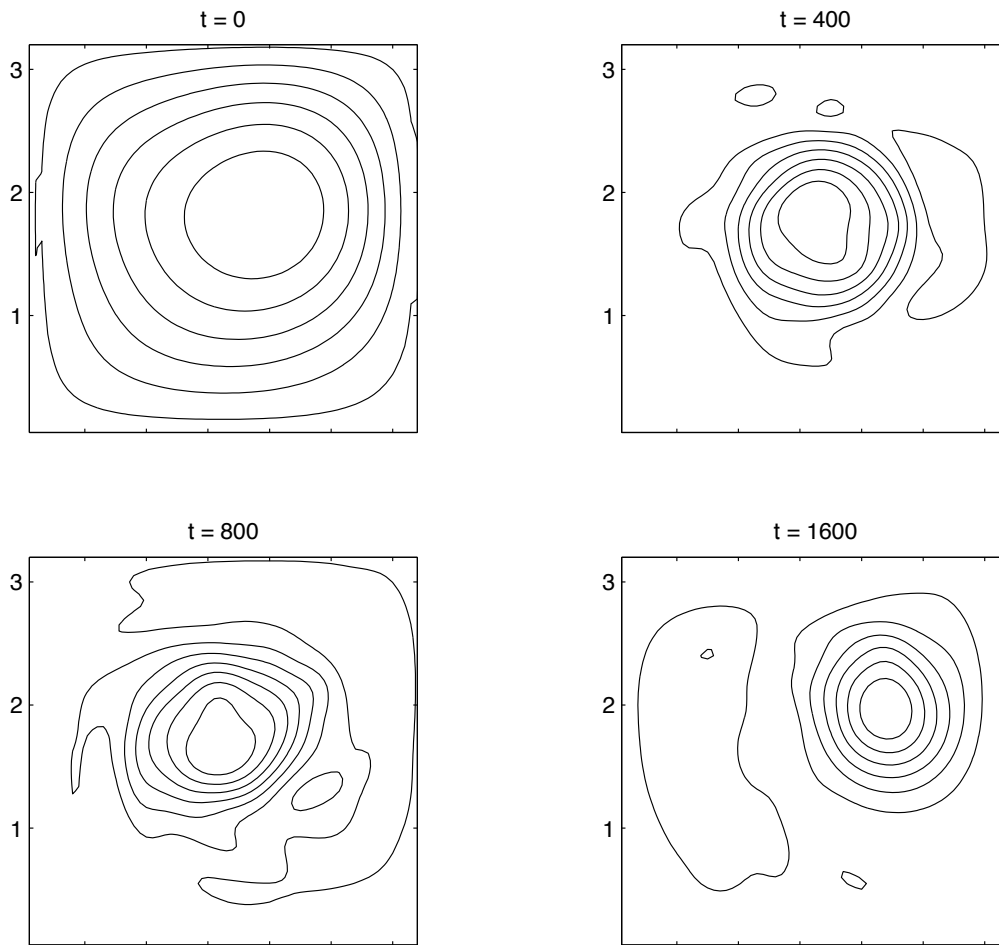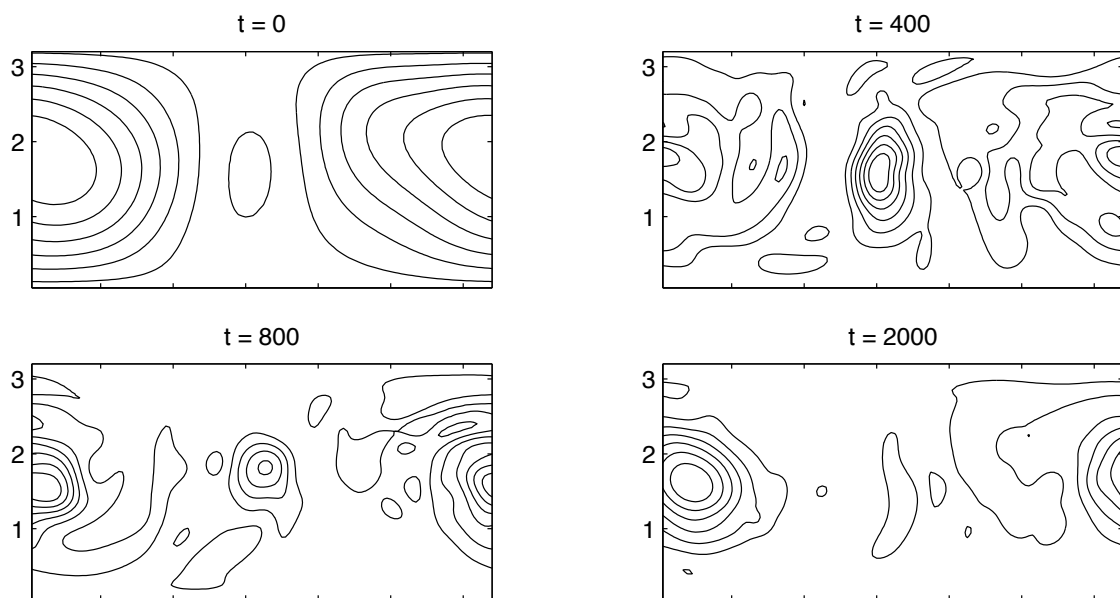
Figure 8: Snapshots of the potential vorticity at $t = 0, 400, 800, 1600$, in the basin during bombardment with localized vortices of alternating sign and amplitude equal to 10% of initial maximal vorticity.
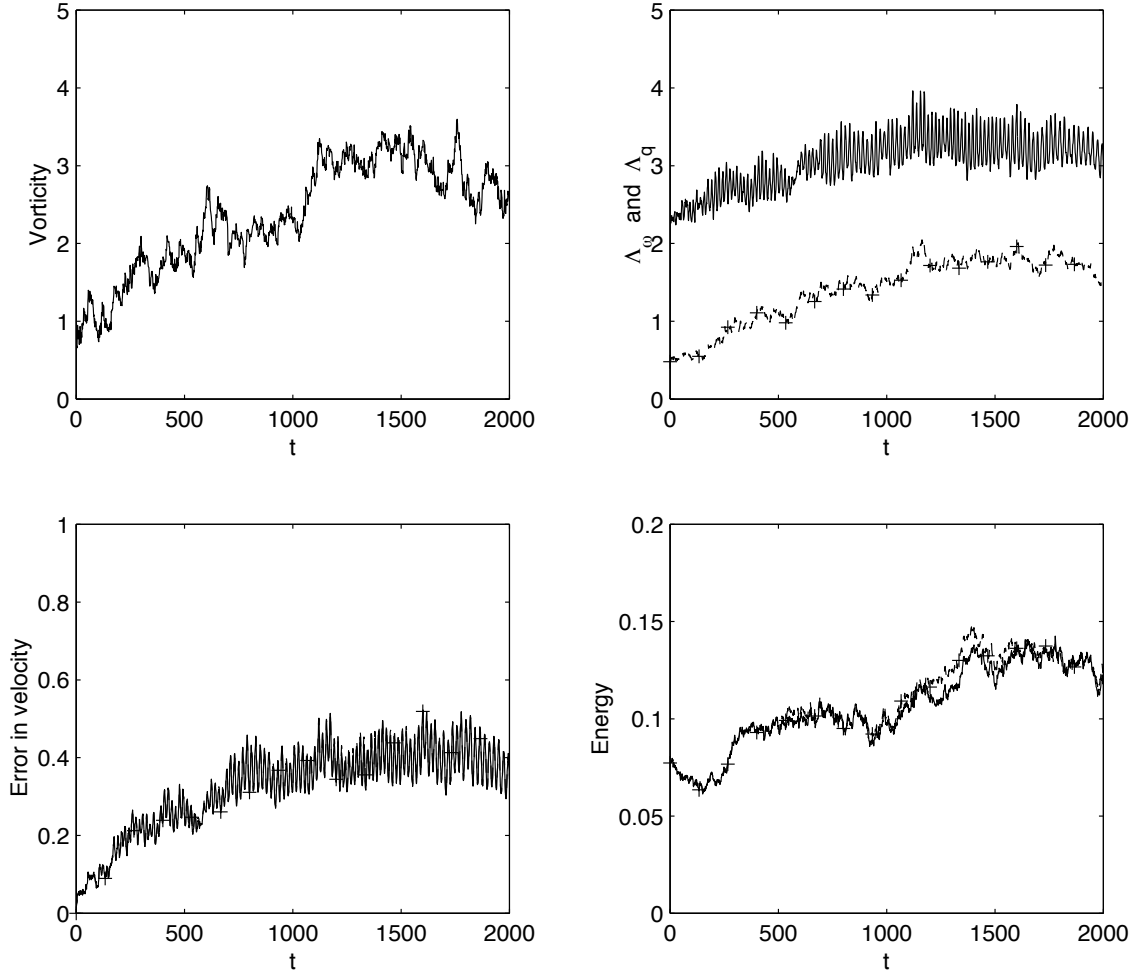
Figure 9: Comparison with crude closure dynamics during bombardment with localized vortices of alternating sign and amplitude equal to 10% of initial maximal vorticity. Top left: maximal potential vorticity $|q|_{\max}$; top right: Λ_ω (plain) and Λ_q $(+ - +)$; bottom left: relative errors in matched velocity $\mathrm{Err}(\vec{v}, \vec{v}^*)$ (plain) and predicted velocity $\mathrm{Err}(\vec{v}, \bar{\vec{v}})$ $(+ - +)$; bottom right: energy E (plain) and predicted energy $\bar{E}$ $(+ - +)$.
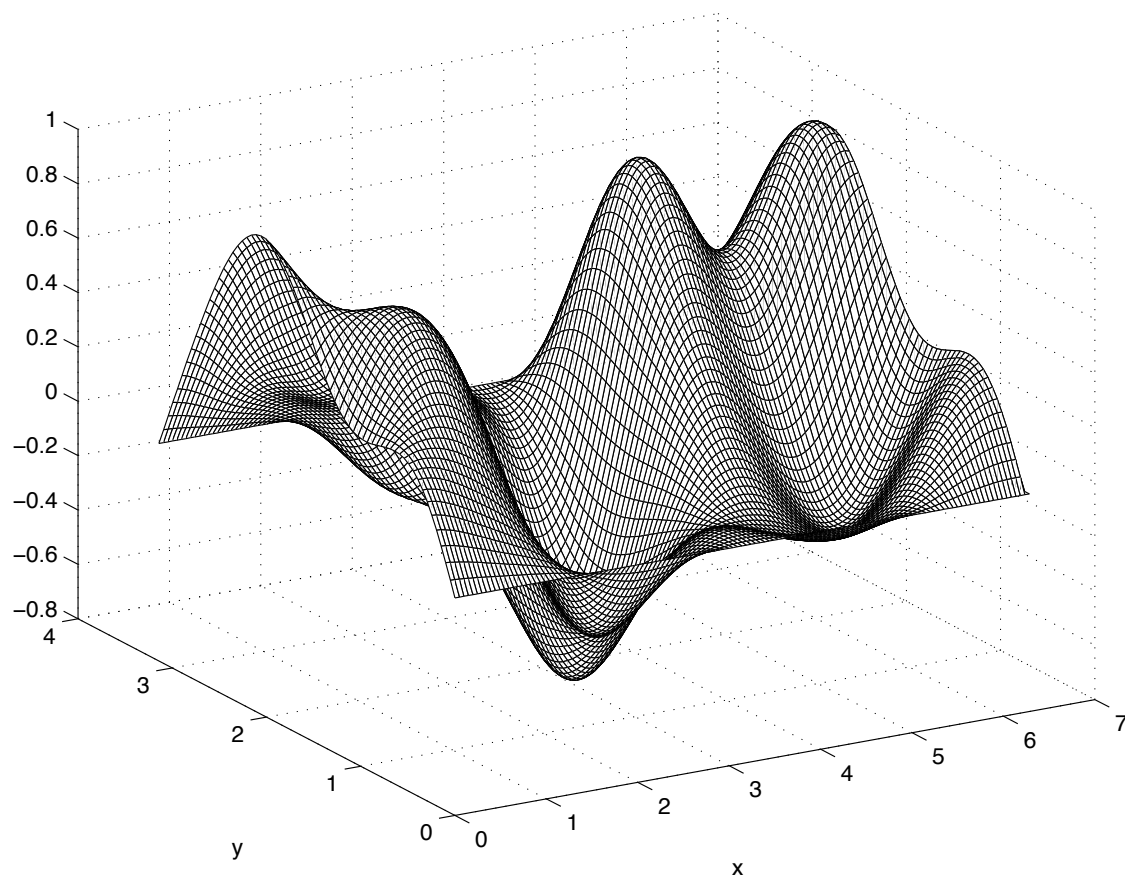
Figure 10: Random topography in the channel.

Figure 11: Snapshots of the potential vorticity at $t = 0, 1, 5, 10, 50, 2000$, during spin-up from zero in the channel, with $H = 1$ and $\nu = 0.01$.

Figure 12: Comparison with crude closure dynamics during spin-up from zero in the channel, with $H = 1$ and $\nu = 0.01$. Top left: energy E (plain) and predicted energy $\bar{E}$ $(+ - +)$; top right: enstrophy $\mathcal{E}$; middle left: relative errors in matched velocity $\mathrm{Err}(\vec{v}, \vec{v}^*)$ (plain) and predicted velocity $\mathrm{Err}(\vec{v}, \bar{\vec{v}})$ $(+ - +)$; middle right: relative errors in matched potential vorticity $\mathrm{Err}(q, q^*)$ (plain) and predicted potential vorticity $\mathrm{Err}(q, \bar{q})$ $(+ - +)$; bottom left: correlation $\mathrm{Corr}(q, \psi)$; bottom right: Λ_ω (plain) and Λ_q $(+ - +)$.

Figure 13: Snapshots of the potential vorticity at $t = 0, 400, 800, 2000$, in the channel during bombardment with localized vortices of alternating sign and amplitude equal to 10% of initial maximal vorticity.
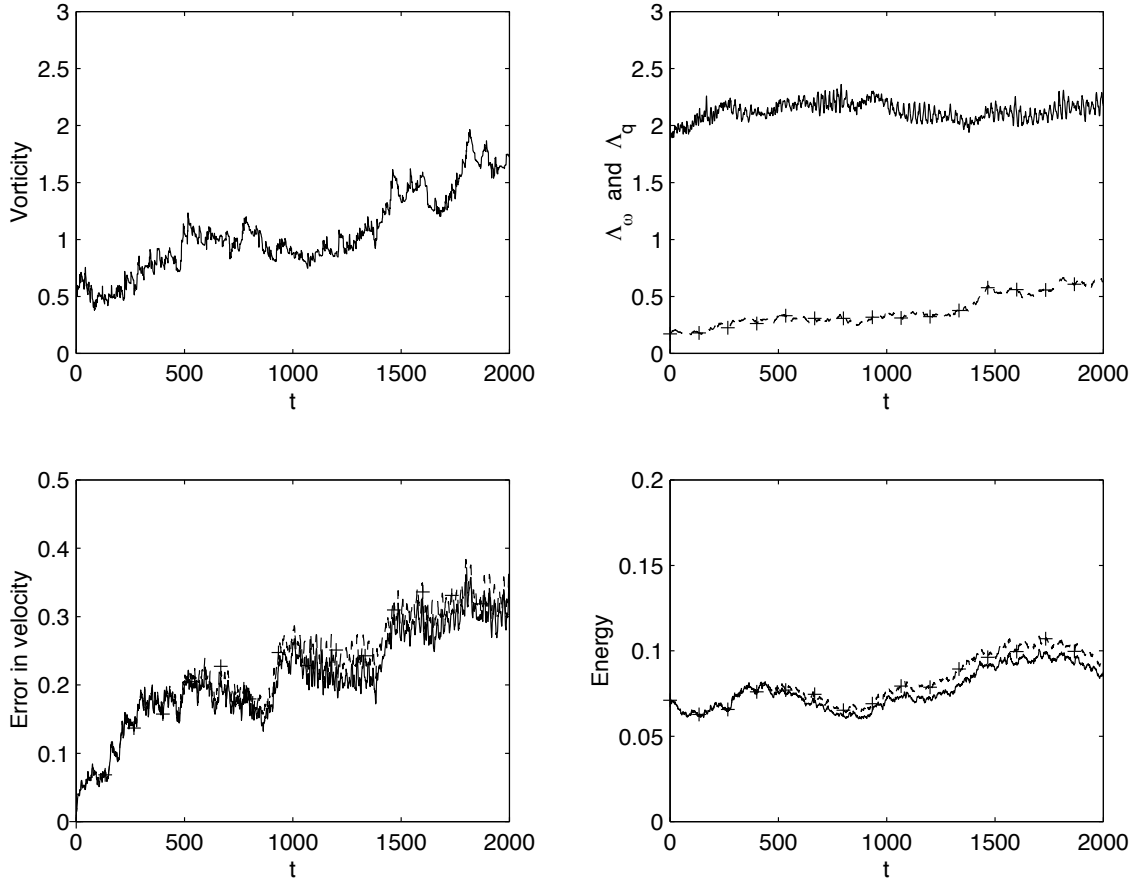
Figure 14: Comparison with crude closure dynamics during bombardment with localized vortices of alternating sign and amplitude equal to 10% of initial maximal vorticity. Top left: maximal potential vorticity $|q|_{\max}$; top right: Λ_ω (plain) and Λ_q $(+ - +)$; bottom left: relative errors in matched velocity $\mathrm{Err}(\vec{v}, \vec{v}^*)$ (plain) and predicted velocity $\mathrm{Err}(\vec{v}, \bar{\vec{v}})$ $(+ - +)$; bottom right: energy E (plain) and predicted energy $\bar{E}$ $(+ - +)$.
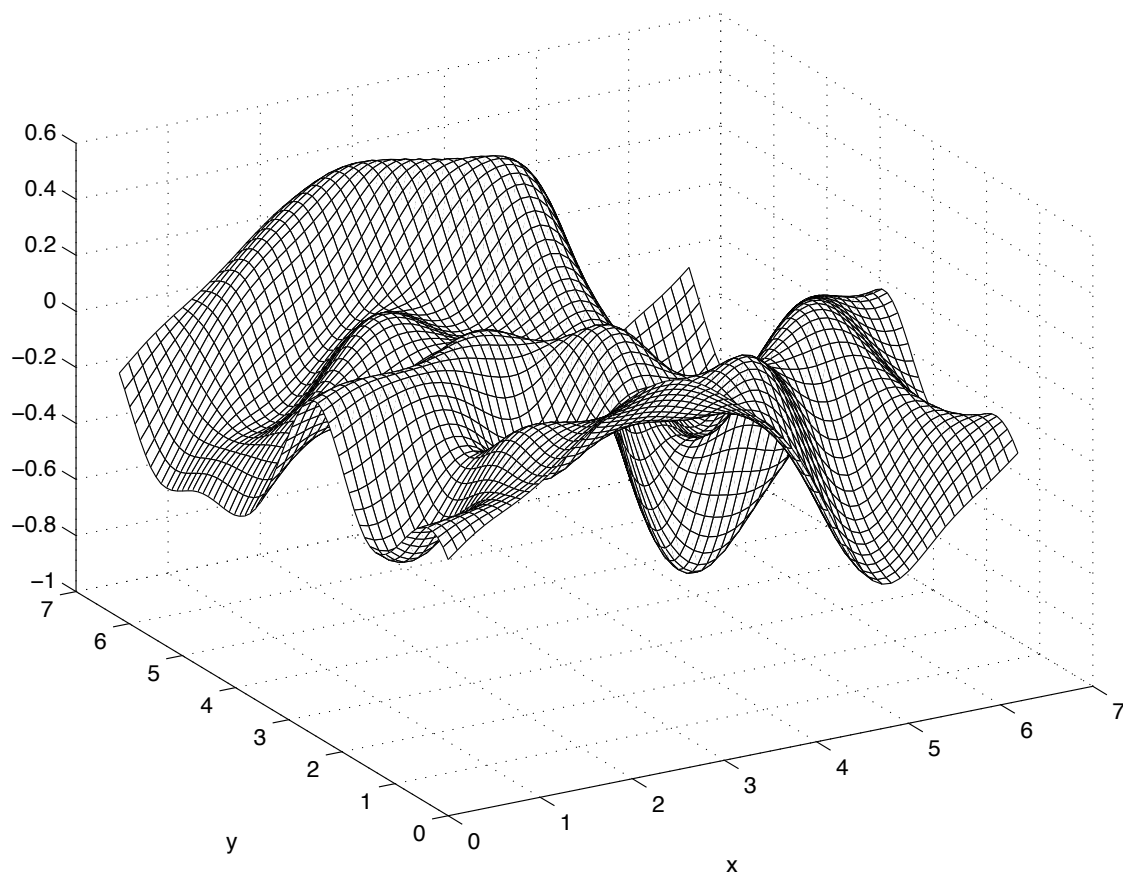
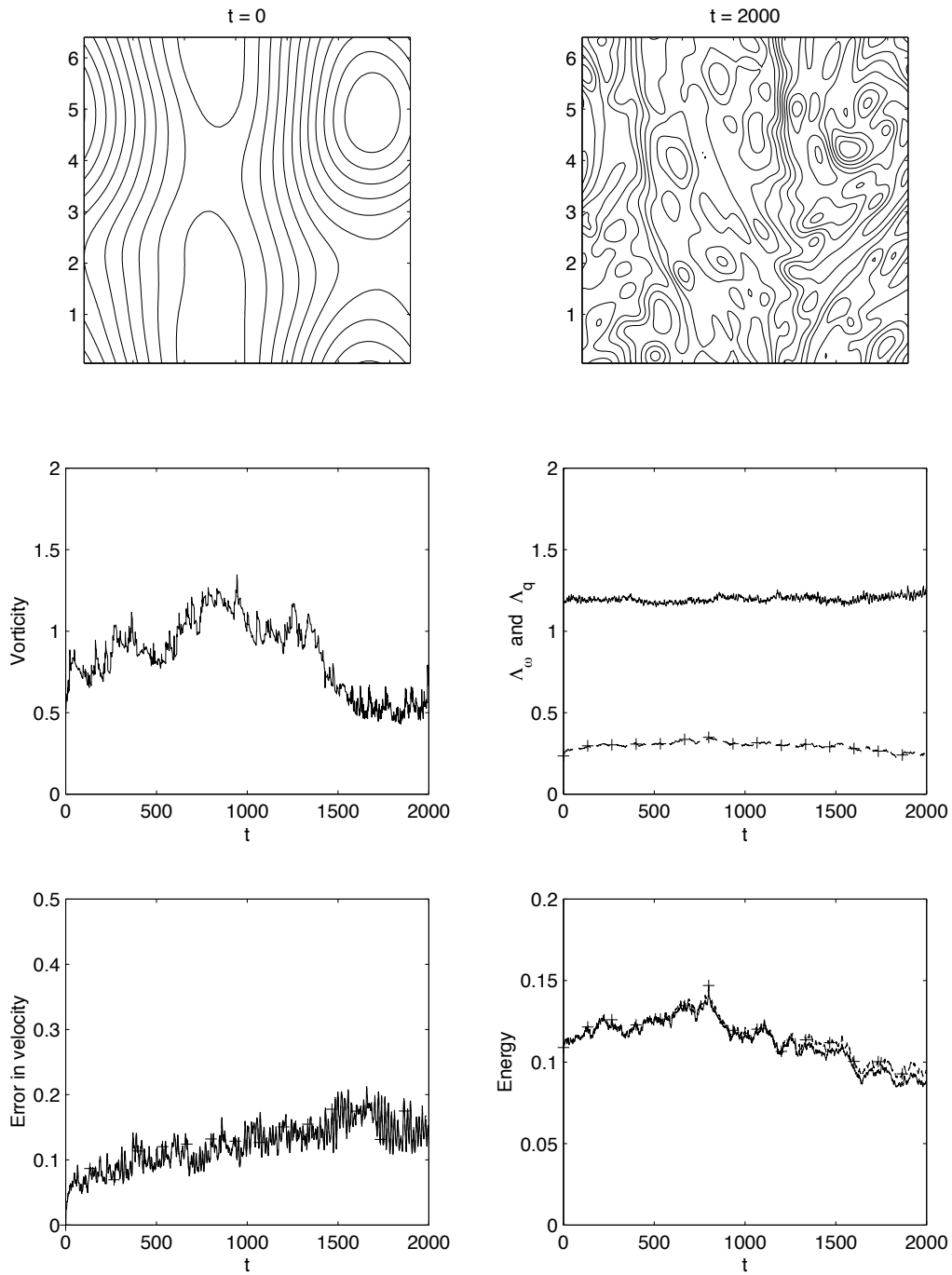Figure 15: Random topography on the torus.

Figure 16: Comparison with crude closure dynamics during bombardment with dipolar vortices of amplitude equal to 10% of initial maximal vorticity, with $\mu_0 = -1$. Top: snapshots of potential vorticity at $t = 0$ and $t = 2000$; middle left: maximal potential vorticity $|q|_{\max}$; middle right: Λ_ω (plain) and Λ_q $(+ - +)$; bottom left: relative errors in matched velocity $\mathrm{Err}(\vec{v}, \vec{v}^*)$ (plain) and predicted velocity $\mathrm{Err}(\vec{v}, \bar{\vec{v}})$ $(+ - +)$; bottom right: energy E (plain) and predicted energy $\bar{E}$ $(+ - +)$.
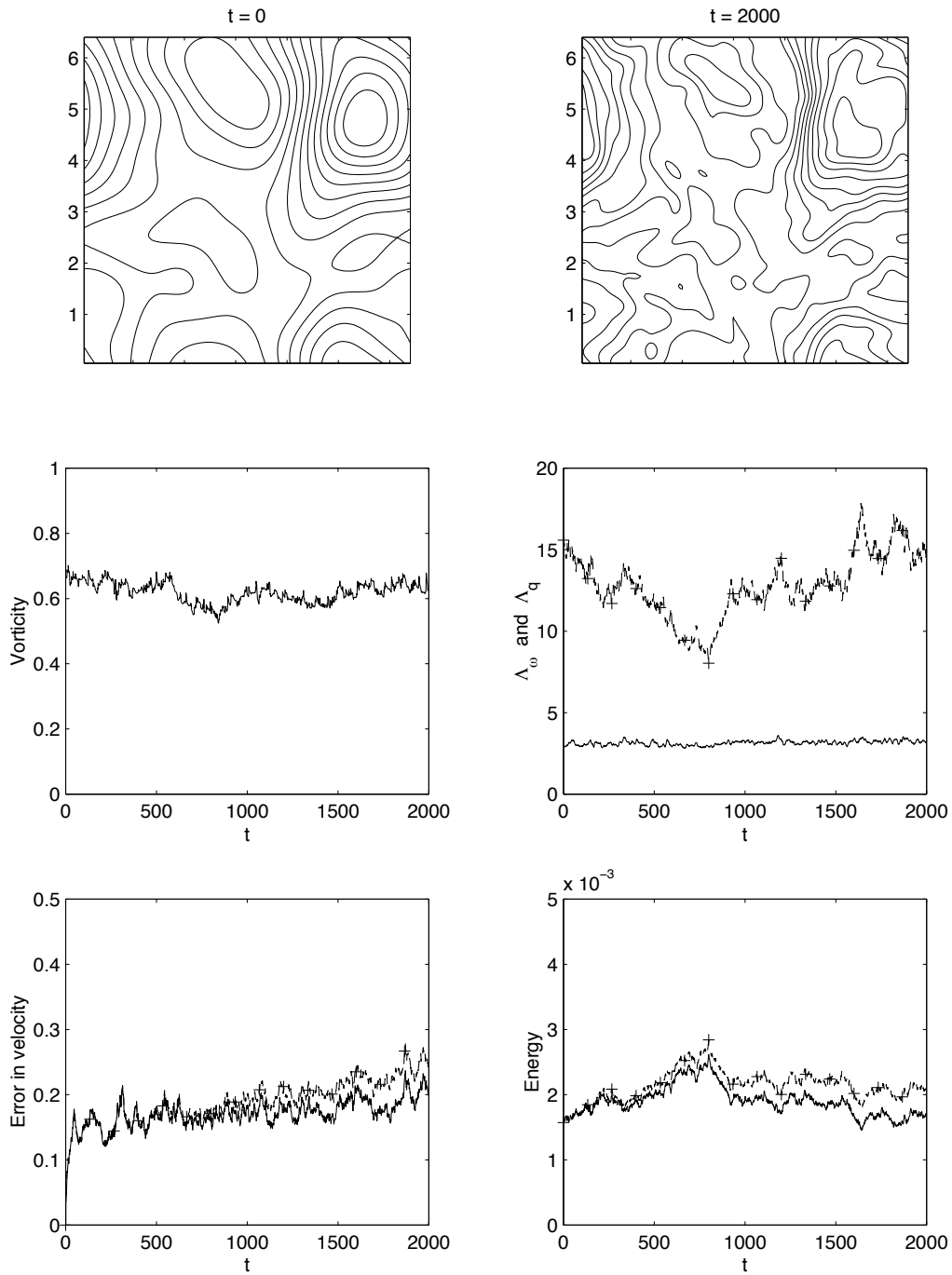
Figure 17: Comparison with crude closure dynamics during bombardment with dipolar vortices of amplitude equal to 10% of initial maximal vorticity, with $\mu_0 = 5$. Top: snapshots of potential vorticity at $t = 0$ and $t = 2000$; middle left: maximal potential vorticity $|q|_{\max}$; middle right: Λ_ω (plain) and Λ_q $(+ - +)$; bottom left: relative errors in matched velocity $\mathrm{Err}(\vec{v}, \vec{v}^*)$ (plain) and predicted velocity $\mathrm{Err}(\vec{v}, \vec{\bar{v}})$ $(+ - +)$; bottom right: energy E (plain) and predicted energy $\bar{E}$ $(+ - +)$.
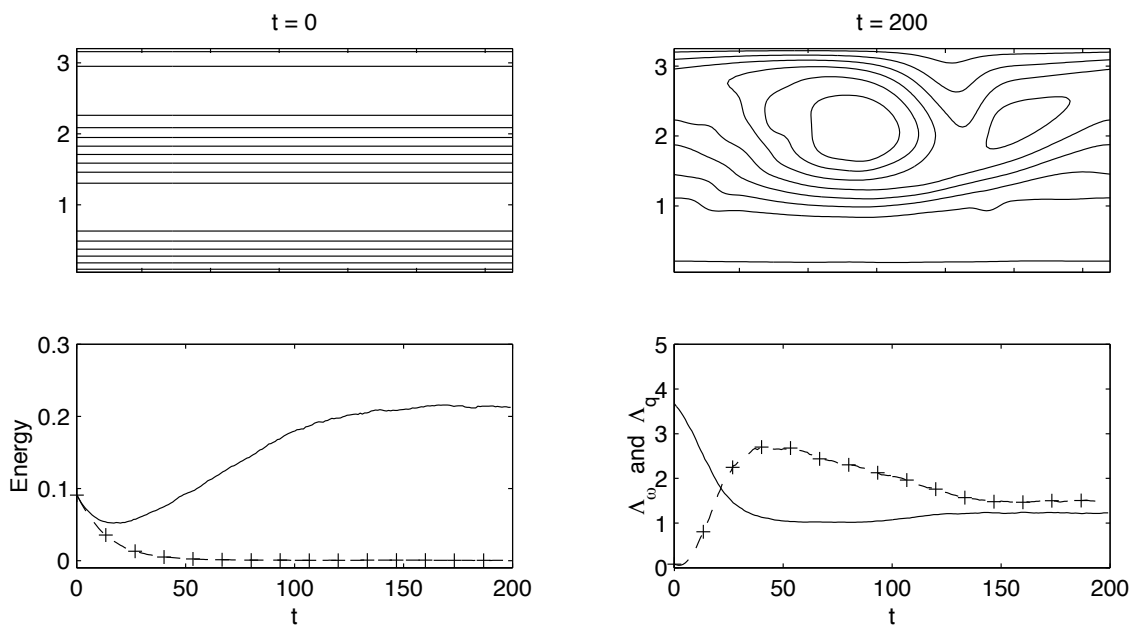
Figure 18: Comparison with crude closure dynamics during bombardment with clockwise vortices of amplitude equal to 12% of initial maximal vorticity, with $\mu_0 = -0.5$, over tall, layered, two-mode topography. Top: snapshots of potential vorticity at $t = 0$ and $t = 200$; bottom left: energy E (plain) and predicted energy $\bar{E}$ $(+-+)$; bottom right: Λ_ω (plain) and Λ_q $(+-+)$.
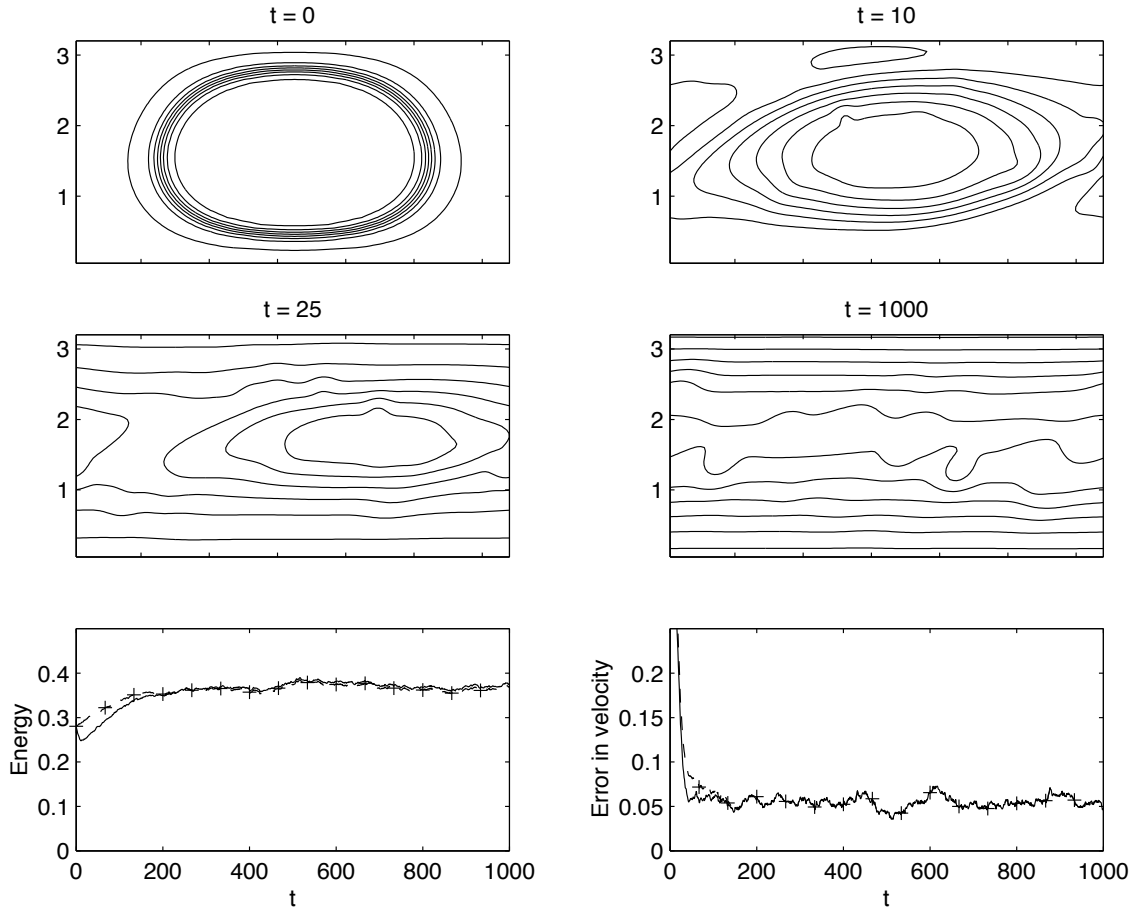
Figure 19: Comparison with crude closure dynamics during bombardment with clockwise vortices of amplitude equal to 8% of initial maximal vorticity, with low amplitude, layered, two-mode topography and the initial conditions set to a Langevin entropy maximizer. Top: snapshots of potential vorticity at $t = 0$ and $t = 10$; Middle: snapshots of potential vorticity at $t = 25$ and $t = 1000$; bottom left: energy E (plain) and predicted energy $\bar{E}$ $(+ - +)$; bottom right: relative errors in matched velocity $\mathrm{Err}(\vec{v}, \vec{v}^*)$ (plain) and predicted velocity $\mathrm{Err}(\vec{v}, \bar{\vec{v}})$ $(+ - +)$.
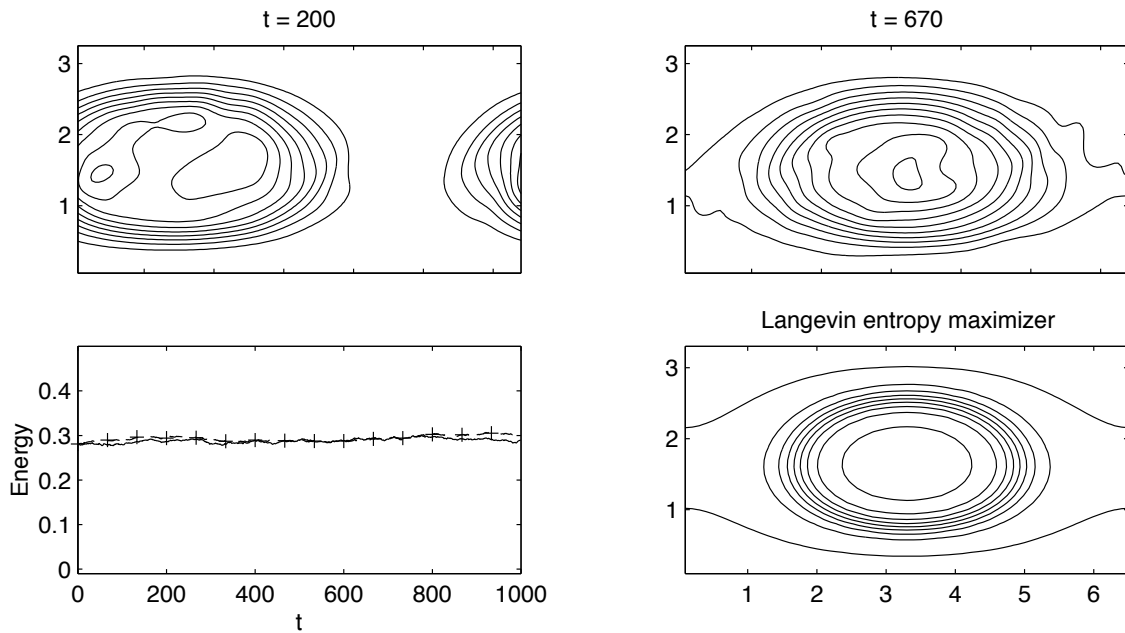
Figure 20: Evolution of Langevin mean-field state during bombardment with localized vortices of alternating sign and amplitude equal to 5% of initial maximal vorticity, with low amplitude, layered, two-mode topography and the initial conditions set to the Langevin entropy maximizer (see Figure 18). Top: snapshots of potential vorticity at $t = 200$ and $t = 670$; bottom left: energy E (plain) and predicted energy $\bar{E}$ $(+ - +)$; bottom right: Langevin entropy maximizing mean-field potential vorticity, q^*, with E, Γ, Q, and $\bar{Q}$ matched from exact solution at $t = 670$ (top right). Note: contour lines at identical levels in above three frames.

Research Reports

No.	Authors	Title
99-02	M.J. Grote, A.J. Majda	Crude Closure for Flow with Topography Through Large Scale Statistical Theory
99-01	A.M. Matache, I. Babuška, C. Schwab	Generalized p-FEM in Homogenization
98-10	J.M. Melenk, C. Schwab	The hp Streamline Diffusion Finite Element Method for Convection Dominated Problems in one Space Dimension
98-09	M.J. Grote	Nonreflecting Boundary Conditions For Electromagnetic Scattering
98-08	M.J. Grote, J.B. Keller	Exact Nonreflecting Boundary Condition For Elastic Waves
98-07	C. Lage	Concept Oriented Design of Numerical Software
98-06	N.P. Hancke, J.M. Melenk, C. Schwab	A Spectral Galerkin Method for Hydrodynamic Stability Problems
98-05	J. Waldvogel	Long-Term Evolution of Coorbital Motion
98-04	R. Sperb	An alternative to Ewald sums, Part 2: The Coulomb potential in a periodic system
98-03	R. Sperb	The Coulomb energy for dense periodic systems
98-02	J.M. Melenk	On n-widths for Elliptic Problems
98-01	M. Feistauer, C. Schwab	Coupling of an Interior Navier–Stokes Problem with an Exterior Oseen Problem
97-20	R.L. Actis, B.A. Szabo, C. Schwab	Hierarchic Models for Laminated Plates and Shells
97-19	C. Schwab, M. Suri	Mixed hp Finite Element Methods for Stokes and Non-Newtonian Flow
97-18	K. Gerdes, D. Schötzau	hp FEM for incompressible fluid flow - stable and stabilized
97-17	L. Demkowicz, K. Gerdes, C. Schwab, A. Bajer, T. Walsh	HP90: A general & flexible Fortran 90 hp-FE code
97-16	R. Jeltsch, P. Klingenstein	Error Estimators for the Position of Discontinuities in Hyperbolic Conservation Laws with Source Terms which are solved using Operator Splitting
97-15	C. Lage, C. Schwab	Wavelet Galerkin Algorithms for Boundary Integral Equations
97-14	D. Schötzau, C. Schwab, R. Stenberg	Mixed hp - FEM on anisotropic meshes II: Hanging nodes and tensor products of boundary layer meshes